Statistical analysis

Unless otherwise stated, data are represented as means ± SD of at least three determinations. We used an unpaired *t*-test, one-way analysis of variance followed by Dunnett's test for statistical analyses. Values of $P < 0.05$ (indicated as asterisks in figures) were considered statistically significant.

SUPPLEMENTARY MATERIAL

Supplementary Material is available at *HMG* Online.

ACKNOWLEDGEMENTS

We thank Ms H. Otake for her technical assistance.

Conflict of Interest statement. None declared.

FUNDING

This work was supported by Grant-in-Aid for Priority Areas 18077015 (to S.W.), Grants-in-Aid 19390080, 17659241 (to S.W.), 18590796 (Y.I.) and a Grant for the Cooperative Link for Unique Science and Technology for Economy Revitalization (S.W.) from the Ministry of Education, Culture, Sports, Science and Technology of Japan, a grant for the Promotion of Fundamental Studies in Health Sciences of National Institute of Biomedical Innovation (NIBIO), research grants for Cardiovascular Diseases (17A-1) (S.W.) and for Nervous and Mental Disorders (16B-2 and 19A-7) from the Ministry of Health, Labor, and Welfare (to Y.I.), and grants from Takeda Science Foundation (to Y.I.) and the Salt Science Research Foundation, No. 0737 (to S.W.).

REFERENCES

1. Duclos, F., Straub, V., Moore, S.A., Venzke, D.P., Hrstka, R.F., Crosbie, R.H., Durbeej, M., Lebakken, C.S., Ettinger, A.J., van der Meulen, J. *et al.* (1998) Progressive muscular dystrophy in alpha-sarcoglycan-deficient mice. *J. Cell Biol.*, **142**, 1461–1471.
2. Campbell, K.P. (1995) Three muscular dystrophies: loss of cytoskeleton-extracellular matrix linkage. *Cell*, **80**, 675–679.
3. Nigro, V., Okazaki, Y., Belsito, A., Piluso, G., Matsuda, Y., Politano, L., Nigro, G., Ventura, C., Abbondanza, C., Molinari, A.M. *et al.* (1997) Identification of the Syrian hamster cardiomyopathy gene. *Hum. Mol. Genet.*, **6**, 601–607.
4. Campbell, K.P. and Kahl, S.D. (1989) Association of dystrophin and an integral membrane glycoprotein. *Nature*, **338**, 259–262.
5. Tinsley, J.M., Blake, D.J., Zuellig, R.A. and Davies, K.E. (1994) Increasing complexity of the dystrophin-associated protein complex. *Proc. Natl Acad. Sci. USA*, **91**, 8307–8313.
6. Ervasti, J.M. and Campbell, K.P. (1993) A role for the dystrophin–glycoprotein complex as a transmembrane linker between laminin and actin. *J. Cell Biol.*, **122**, 809–823.
7. Turner, P.R., Westwood, T., Regen, C.M. and Steinhardt, R.A. (1988) Increased protein degradation results from elevated free calcium levels found in muscle from mdx mice. *Nature*, **335**, 735–738.
8. Spencer, M.J., Croall, D.E. and Tidball, J.G. (1995) Calpains are activated in necrotic fibers from mdx dystrophic mice. *J. Biol. Chem.*, **270**, 10909–10914.
9. MacLennan, P.A., McArdle, A. and Edwards, R.H. (1991) Effects of calcium on protein turnover of incubated muscles from mdx mice. *Am. J. Physiol.*, **260**, E594–E598.
10. Mallouk, N., Jacquemond, V. and Allard, B. (2000) Elevated subsarcolemmal Ca^{2+} in mdx mouse skeletal muscle fibers detected with Ca^{2+}-activated K^+ channels. *Proc. Natl Acad. Sci. USA*, **97**, 4950–4955.
11. Robert, V., Massimino, M.L., Tosello, V., Marsault, R., Cantini, M., Sorrentino, V. and Pozzan, T. (2001) Alteration in calcium handling at the subcellular level in mdx myotubes. *J. Biol. Chem.*, **276**, 4647–4651.
12. Fong, P.Y., Turner, P.R., Denetclaw, W.F. and Steinhardt, R.A. (1990) Increased activity of calcium leak channels in myotubes of Duchenne human and mdx mouse origin. *Science*, **250**, 673–676.
13. Nakamura, T.Y., Iwata, Y., Sampaolesi, M., Hanada, H., Saito, N., Artman, M., Coetzee, W.A. and Shigekawa, M. (2001) Stretch-activated cation channels in skeletal muscle myotubes from sarcoglycan-deficient hamsters. *Am. J. Physiol. Cell Physiol.*, **281**, C690–C699.
14. Vandebrouck, C., Martin, D., Colson-Van Schoor, M., Debaix, H. and Gailly, P. (2002) Involvement of TRPC in the abnormal calcium influx observed in dystrophic (mdx) mouse skeletal muscle fibers. *J. Cell Biol.*, **158**, 1089–1096.
15. Iwata, Y., Katanosaka, Y., Shijun, Z., Kobayashi, Y., Hanada, H., Shigekawa, M. and Wakabayashi, S. (2005) Protective effects of Ca^{2+} handling drugs against abnormal Ca^{2+} homeostasis and cell damage in myopathic skeletal muscle cells. *Biochem. Pharmacol.*, **70**, 740–751.
16. Iwata, Y., Katanosaka, Y., Arai, Y., Komamura, K., Miyatake, K. and Shigekawa, M. (2003) A novel mechanism of myocyte degeneration involving the Ca^{2+}-permeable growth factor-regulated channel. *J. Cell Biol.*, **161**, 957–967.
17. Nilius, B., Owsianik, G., Voets, T. and Peters, J.A. (2007) Transient receptor potential cation channels in disease. *Physiol. Rev.*, **87**, 165–217.
18. Venkatachalam, K. and Montell, C. (2007) TRP channels. *Annu. Rev. Biochem.*, **76**, 387–417.
19. Clapham, D.E., Julius, D., Montell, C. and Schultz, G. (2005) International Union of Pharmacology. XLIX. Nomenclature and structure-function relationships of transient receptor potential channels. *Pharmacol. Rev.*, **57**, 427–450.
20. Nilius, B., Vennekens, R., Prenen, J., Hoenderop, J.G., Droogmans, G. and Bindels, R.J. (2001) The single pore residue Asp542 determines Ca^{2+} permeation and Mg^{2+} block of the epithelial Ca^{2+} channel. *J. Biol. Chem.*, **276**, 1020–1025.
21. Garcia-Martinez, C., Morenilla-Palao, C., Planells-Cases, R., Merino, J.M. and Ferrer-Montiel, A. (2000) Identification of an aspartic residue in the P-loop of the vanilloid receptor that modulates pore properties. *J. Biol. Chem.*, **275**, 32552–32558.
22. Kanzaki, M., Zhang, Y.Q., Mashima, H., Li, L., Shibata, H. and Kojima, I. (1999) Translocation of a calcium-permeable cation channel induced by insulin-like growth factor-I. *Nat. Cell Biol.*, **1**, 165–170.
23. Wehling, M., Spencer, M.J. and Tidball, J.G. (2001) A nitric oxide synthase transgene ameliorates muscular dystrophy in mdx mice. *J. Cell Biol.*, **155**, 123–131.
24. Garcia-Sanz, N., Fernandez-Carvajal, A., Morenilla-Palao, C., Planells-Cases, R., Fajardo-Sanchez, E., Fernandez-Ballester, G. and Ferrer-Montiel, A. (2004) Identification of a tetramerization domain in the C terminus of the vanilloid receptor. *J. Neurosci.*, **24**, 5307–5314.
25. Hellwig, N., Albrecht, N., Harteneck, C., Schultz, G. and Schaefer, M. (2005) Homo- and heteromeric assembly of TRPV channel subunits. *J. Cell Sci.*, **118**, 917–928.
26. Lee, E.H., Kim do, H. and Allen, P.D. (2006) Interplay between intra- and extracellular calcium ions. *Mol. Cells*, **21**, 315–329.
27. Nagasawa, M., Nakagawa, Y., Tanaka, S. and Kojima, I. (2007) Chemotactic peptide fMetLeuPhe induces translocation of the TRPV2 channel in macrophages. *J. Cell. Physiol.*, **210**, 692–702.
28. Iwata, Y., Katanosaka, Y., Hisamitsu, T. and Wakabayashi, S. (2007) Enhanced Na^+/H^+ exchange activity contributes to the pathogenesis of muscular dystrophy via involvement of P2 receptors. *Am. J. Pathol.*, **171**, 1576–1587.
29. Perrone, C.E., Fenwick-Smith, D. and Vandenburgh, H.H. (1995) Collagen and stretch modulate autocrine secretion of insulin-like growth factor-1 and insulin-like growth factor binding proteins from differentiated skeletal muscle cells. *J. Biol. Chem.*, **270**, 2099–2106.
30. Fadic, R. (2005) Cell surface and gene expression regulation molecules in dystrophinopathy: mdx vs. Duchenne. *Biol. Res.*, **38**, 375–380.
31. Saito, M., Hanson, P.I. and Schlesinger, P. (2007) Luminal chloride-dependent activation of endosome calcium channels: patch clamp study of enlarged endosomes. *J. Biol. Chem.*, **282**, 27327–27333.
32. Bassel-Duby, R. and Olson, E.N. (2006) Signaling pathways in skeletal muscle remodeling. *Annu. Rev. Biochem.*, **75**, 19–37.

33. Crawford, G.E., Faulkner, J.A., Crosbie, R.H., Campbell, K.P., Froehner, S.C. and Chamberlain, J.S. (2000) Assembly of the dystrophin-associated protein complex does not require the dystrophin COOH-terminal domain. *J. Cell Biol.*, **150**, 1399–1410.
34. Iwata, Y., Pan, Y., Hanada, H., Yoshida, T. and Shigekawa, M. (1996) Dystrophin–glycoprotein complex purified from hamster cardiac muscle. Comparison of the complexes from cardiac and skeletal muscles of hamster and rabbit. *J. Mol. Cell. Cardiol.*, **28**, 2501–2509.
35. Rando, T.A. and Blau, H.M. (1994) Primary mouse myoblast purification, characterization, and transplantation for cell-mediated gene therapy. *J. Cell Biol.*, **125**, 1275–1287.
36. Naruse, K., Yamada, T. and Sokabe, M. (1998) Involvement of SA channels in orienting response of cultured endothelial cells to cyclic stretch. *Am. J. Physiol.*, **274**, H1532–H1538.
37. Grynkiewicz, G., Poenie, M. and Tsien, R.Y. (1985) A new generation of Ca^{2+} indicators with greatly improved fluorescence properties. *J. Biol. Chem.*, **260**, 3440–3450.

Biophysical Journal Volume 97 November 2009 2674–2683

A Model of Na^+/H^+ Exchanger and Its Central Role in Regulation of pH and Na^+ in Cardiac Myocytes

Chae Young Cha,[†‡] Chiaki Oka,[‡] Yung E. Earm,[§] Shigeo Wakabayashi,[¶] and Akinori Noma[†*]

[†]Biosimulation Project, Faculty of Bioinformatics, Ritsumeikan University, Kusatsu, Japan; [‡]Biosimulation Project, Graduate School of Medicine, Kyoto University, Kyoto, Japan; [§]Department of Physiology, Seoul National University, Seoul, Korea; and [¶]Department of Molecular Physiology, National Cardiovascular Center Research Institute, Osaka, Japan

ABSTRACT A new kinetic model of the Na^+/H^+ exchanger (NHE) was developed by fitting a variety of major experimental findings, such as ion-dependencies, forward/reverse mode, and the turnover rate. The role of NHE in ion homeostasis was examined by implementing the NHE model in a minimum cell model including intracellular pH buffer, Na^+/K^+ pump, background H^+, and Na^+ fluxes. This minimum cell model was validated by reconstructing recovery of pH_i from acidification, accompanying transient increase in $[Na^+]_i$ due to NHE activity. Based on this cell model, steady-state relationships among pH_i, $[Na^+]_i$, and $[Ca^{2+}]_i$ were quantitatively determined, and thereby the critical level of acidosis for cell survival was predicted. The acidification reported during partial blockade of the Na^+/K^+ pump was not attributed to a dissipation of the Na^+ gradient across the membrane, but to an increase in indirect H^+ production. This NHE model, though not adapted to the dimeric behavioral aspects of NHE, can provide a strong clue to quantitative prediction of degree of acidification and accompanying disturbance of ion homeostasis under various pathophysiological conditions.

INTRODUCTION

Several types of pH-related transporters are present in the sarcolemma of cardiac myocytes. Among them, the Na^+-H^+ exchanger (NHE) is regarded as the main acid extruder, in that its H^+ flux is much larger than that of the other acid extruder, the Na^+-HCO_3^- cotransporter (1,2). In addition, abnormal enhancement of NHE activity under acidosis potentially induces intracellular Na^+ overload through Na^+ influx during pumping out excess H^+ (3) and eventually Ca^{2+} overload by depressing the Na^+-Ca^{2+} exchanger (NCX). For example, the enhanced NHE has been reported to play a critical role in ischemia/reperfusion injury (4,5), and slow force response (6,7). Since regulation of all intracellular H^+, Na^+, and Ca^{2+} concentrations within a physiological range is of vital importance in maintaining the excitability, contractility, and cell volume regulation in cardiac myocytes, a dynamic NHE model is indispensable to investigate mechanisms underlying the cellular ionic homeostasis as well as its failure under pathophysiological conditions using mathematical cell models.

A variety of mathematical models of NHE has been developed. Leem et al. (1) derived an empirical polynomial equation based on their measurements of pH_i-NHE flux relationships, and this model was used for exploring effects of acidosis on contraction and membrane excitation (8,9). NHE activity has also been described with Hill equations (10) or by a simple kinetic model (11) that attributed NHE activation to binding of intracellular H^+ to its modifier site. These simple models were easy to apply, but did not provide any details of the dependencies on the intra- and extracellular concentrations of H^+ and Na^+, except for pH_i. Recently, more-complicated kinetic NHE models have been proposed (12–15), but even the latest NHE model (14) did not take account of extracellular H^+ or Na^+ dependencies. In addition to these classical NHE schemes, model development based on the dimer configuration of NHE (16) has been attempted (17–20). However, these models are quite different from each other and it is still difficult to distinguish them experimentally. Furthermore, in cardiac myocytes no positive proof is demonstrated for the cooperative operation of monomers within the dimeric composition. Thus, there is no available NHE model with sufficient detail to predict the contribution of NHE in intact myocytes.

In this study, we developed an NHE model, which satisfactorily reconstructs the dependencies on the intra- and extracellular concentrations of H^+ and Na^+ reported in the systematic experiments in the Purkinje fiber (21,22), in addition to the experimental findings in the transfected cell line (15). Subsequently, we implemented the new NHE model in a simple cell model, and found that original recordings of pH_i and $[Na^+]_i$ variations in experiments were well explained by the alteration of NHE activity. We then examined the role of NHE under pathophysiological conditions by considering the steady-state relationship between pH_i and $[Na^+]_i$ during depression of active Na^+ transport or during long-lasting acidosis.

METHODS

Development of the NHE model scheme

A variety of kinetic schemes, such as ping-pong (12,13), simultaneous ion-transporting (17,18), or dimer models (19,20) have been suggested for NHE. These model schemes might equally well explain experimental findings.

Submitted November 5, 2008, and accepted for publication August 21, 2009.

*Correspondence: noma@sk.ritsumei.ac.jp

Editor: Michael Pusch.

0006-3495/09/11/2674/10 $2.00

doi: 10.1016/j.bpj.2009.08.053

Because of its applicability to a wide range of experimental data, we adopted a ping-pong scheme with 1:1 stoichiometry. Consideration of the dimeric model schemes is presented in the Supporting Material.

The new kinetic NHE model is composed of two distinct functional units: an ion-exchanging part (j_{exch}) and a proton-modifier part (*Mod*). The H^+ efflux or Na^+ influx through NHE (J_{NHE}) is given by the equation

$$J_{NHE}(\text{mM/ms}) = N \times Mod\left([H^+]_i, [H^+]_o\right) \times j_{exch}\left([H^+]_i, [H^+]_o, [Na^+]_i, [Na^+]_o\right)/(A\, vol_i), \quad (1)$$

where N is the total number of NHE molecules, A is the Avogadro number, and vol_i is the intracellular volume.

The ion-exchanging part (j_{exch})

A ping-pong-type model with $1H^+$:$1Na^+$ stoichiometry (23) can be described with a six- or eight-state model (Fig. 1, *A* or *B*) by assuming that H^+ and Na^+ either can or cannot bind simultaneously to the transporter (23). In the six-state model, the steady-state turnover rate, j_{exch}, is given as

$$j_{exch} = \frac{\dfrac{k_1^+\frac{[Na^+]_o}{K_{Na}^o}}{\left(1+\frac{[Na^+]_o}{K_{Na}^o}+\frac{[H^+]_o}{K_H^o}\right)}\dfrac{k_2^+\frac{[H^+]_i}{K_H^i}}{\left(1+\frac{[Na^+]_i}{K_{Na}^i}+\frac{[H^+]_i}{K_H^i}\right)} - \dfrac{k_1^-\frac{[Na^+]_i}{K_{Na}^i}}{\left(1+\frac{[Na^+]_i}{K_{Na}^i}+\frac{[H^+]_i}{K_H^i}\right)}\dfrac{k_2^-\frac{[H^+]_o}{K_H^o}}{\left(1+\frac{[Na^+]_o}{K_{Na}^o}+\frac{[H^+]_o}{K_H^o}\right)}}{\dfrac{k_1^+\frac{[Na^+]_o}{K_{Na}^o}}{\left(1+\frac{[Na^+]_o}{K_{Na}^o}+\frac{[H^+]_o}{K_H^o}\right)} + \dfrac{k_2^+\frac{[H^+]_i}{K_H^i}}{\left(1+\frac{[Na^+]_i}{K_{Na}^i}+\frac{[H^+]_i}{K_H^i}\right)} + \dfrac{k_1^-\frac{[Na^+]_i}{K_{Na}^i}}{\left(1+\frac{[Na^+]_i}{K_{Na}^i}+\frac{[H^+]_i}{K_H^i}\right)} + \dfrac{k_2^-\frac{[H^+]_o}{K_H^o}}{\left(1+\frac{[Na^+]_o}{K_{Na}^o}+\frac{[H^+]_o}{K_H^o}\right)}}. \quad (2)$$

In the eight-state model, it is given as

$$j_{exch} = \frac{\dfrac{k_1^+\frac{[Na^+]_o}{K_{Na}^o}}{\left(1+\frac{[Na^+]_o}{K_{Na}^o}\right)\left(1+\frac{[H^+]_o}{K_H^o}\right)}\dfrac{k_2^+\frac{[H^+]_i}{K_H^i}}{\left(1+\frac{[Na^+]_i}{K_{Na}^i}\right)\left(1+\frac{[H^+]_i}{K_H^i}\right)} - \dfrac{k_1^-\frac{[Na^+]_i}{K_{Na}^i}}{\left(1+\frac{[Na^+]_i}{K_{Na}^i}\right)\left(1+\frac{[H^+]_i}{K_H^i}\right)}\dfrac{k_2^-\frac{[H^+]_o}{K_H^o}}{\left(1+\frac{[Na^+]_o}{K_{Na}^o}\right)\left(1+\frac{[H^+]_o}{K_H^o}\right)}}{\dfrac{k_1^+\frac{[Na^+]_o}{K_{Na}^o}}{\left(1+\frac{[Na^+]_o}{K_{Na}^o}\right)\left(1+\frac{[H^+]_o}{K_H^o}\right)} + \dfrac{k_2^+\frac{[H^+]_i}{K_H^i}}{\left(1+\frac{[Na^+]_i}{K_{Na}^i}\right)\left(1+\frac{[H^+]_i}{K_H^i}\right)} + \dfrac{k_1^-\frac{[Na^+]_i}{K_{Na}^i}}{\left(1+\frac{[Na^+]_i}{K_{Na}^i}\right)\left(1+\frac{[H^+]_i}{K_H^i}\right)} + \dfrac{k_2^-\frac{[H^+]_o}{K_H^o}}{\left(1+\frac{[Na^+]_o}{K_{Na}^o}\right)\left(1+\frac{[H^+]_o}{K_H^o}\right)}}, \quad (3)$$

where k values are rate constants and the K values are dissociation constants for individual ions. It is assumed that the binding and release of ions are instantaneous, and K values are not affected by binding of Na^+ or H^+ in the eight-state model.

The proton-modifier part (Mod)

Distinct from the ion-exchanging mechanism, NHE has an intracellular H^+-binding step for its activation (15). Since the value of the Hill coefficient (n_H) is still a matter of debate (24,25), we tested n_H values from 1 to 4 in data fitting of a Hill equation:

$$Mod = \frac{1}{1+\dfrac{(K_i)^{n_H}}{([H^+]_i)^{n_H}}}. \quad (4)$$

The pH_i-J_{NHE} relationship shifted in the acidic pH_i direction with decreasing pH_o in cardiac myocytes (21,22,26) and other cell types (24,27). However, the mechanism of depression by the extracellular H^+ has not been determined experimentally. Two mechanisms were considered here. First, the parallel shift may simply result from a competitive interaction between extracellular H^+ and Na^+ in the ion-exchanging part (24). In this case, the *Mod* remains the same as described by Eq. 4. Secondly, the parallel shift might occur when the extracellular H^+ directly modulates the proton-modifier part (Fig. 1 *C*), as expressed by

$$Mod = \frac{1}{1+\left(1+\dfrac{([H^+]_o)^{n_H}}{(K_o)^{n_H}}\right)\dfrac{(K_i)^{n_H}}{([H^+]_i)^{n_H}}}. \quad (5)$$

Mod in the former scheme is designated as *Mod1* (Eq. 4) and the latter as *Mod2* (Eq. 5). The Hill coefficient for extracellular H^+ (n_H) was

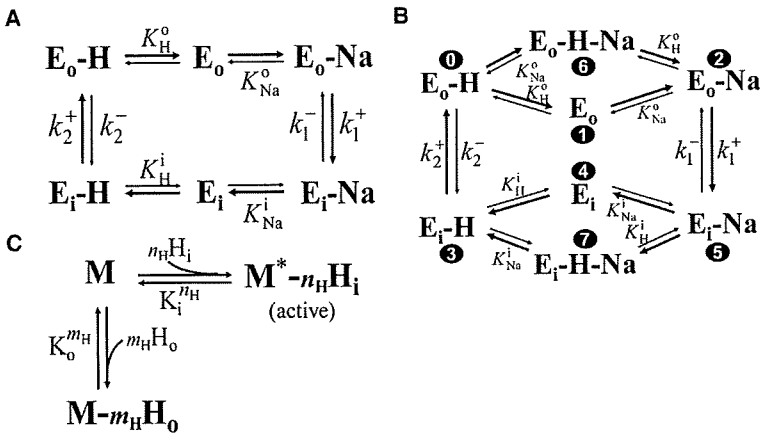

FIGURE 1 Schemes for the NHE model. Schemes for the ion-exchanging part: the six-state model (*A*) and the eight-state model (*B*). E_o represent the state in which the binding cavity opens to the outside of the cell and E_i is the state with the binding cavity open to the inside. The thick arrows indicate the forward direction. Definitions of the parameters are given in Table S1. The numerals in panel *B* indicate state labels that are referred to in Fig. 9 *B*. (*C*) Schemes for the proton-modifier part (M). Ion binding was assumed to be instantaneous with equilibrium constants, the *K* values. The asterisk indicates the state of M that activates E.

assumed to be 1 in this study, based on the experimental finding of $m_H = 1.2$ (21).

When the experimental data were fitted with Eq. 1, j_{exch} of a six- (Eq. 2) or eight-state (Eq. 3) model and *Mod1* (Eq. 4) or *Mod2* (Eq. 5) were examined. Since n_H ranged from 1 to 4, we examined 16 combinations of j_{exch} and *Mod* by data fitting.

Determination of unknown parameters

The ion-exchanging part of the NHE model was expressed as a closed-loop and constrained by the following microscopic reversibility (Eq. 6), leaving nine or 10 unknown parameters to be determined (see Table S1 in the Supporting Material):

$$\frac{K_H^i K_{Na}^o}{K_H^o K_{Na}^i} = \frac{k_1^+ k_2^+}{k_1^- k_2^-}. \tag{6}$$

Methods of fitting

The Levenberg-Marquardt fitting method was used to search for a minimum of chi-square (χ^2),

$$\chi^2 = \sum_{m=1}^{M} \left(\frac{y_m - y(x_m)}{\sigma_m} \right)^2, \tag{7}$$

where M is size of data set, y_m is experimental data of J_{NHE}, $y(x_m) = J_{NHE}([H^+]_i, [H^+]_o, [Na^+]_i$, or $[Na^+]_o)$ defined by Eq. 1 and σ_m is standard deviation (SD) for the m^{th} data point. We found that the χ^2 function of J_{NHE} had numerous local minimums in 9- or 10-dimensional parameter space. Therefore, local minimums were searched with initial values which were varied systematically within a physiological range (see Table S1), and then the least χ^2 was selected among them. The interval for varying initial values should be small enough to avoid missing the global minimum of the χ^2 function. As a compromise with computational cost, 3,674,160 starting points were used in each model scheme. Further consideration of the fitting method was presented in the Supporting Material.

Experimental data for determining model parameters

Selection of relevant experimental data is critical for constructing a precise model. We used three kinds of experimental data: the amplitude of J_{NHE} at various combinations of ($[H^+]_i$, $[H^+]_o$, $[Na^+]_i$, or $[Na^+]_o$), forward/reverse mode of ionic exchange, and the NHE turnover rate.

The measurements of NHE vary due to recording techniques (ion selective electrode or fluorescent dye) or differences in specimens (species (2), and muscles or isolated cells (28)). To minimize the experimental variations, systematic data were collected in sheep Purkinje fibers from two articles published by the same group (21,22) in which their established experimental methods were used. Alternatively, the experimental data from single ventricular myocytes might be adopted. As far as we compared, however, the configuration of pH_i-, pH_o-, and $[Na^+]_o$-J_{NHE} relationships obtained in dissociated ventricular myocyte were largely comparable to those in Purkinje fiber (see the Supporting Material). Furthermore, no measurement of $[Na^+]_i$-J_{NHE} relationship was available in ventricular myocytes. Therefore, we considered that the use of Purkinje fiber data was appropriate.

Despite the identical experimental methods in Purkinje fibers, NHE flux was still quite variable among different preparations. To fit the data set simultaneously, the amplitude of J_{NHE} was normalized with reference to common pH_i, pH_o, $[Na^+]_i$, and $[Na^+]_o$ in individual results. We assumed that the major subtype was NHE1 in Purkinje fibers (29) and that the diversity of NHE flux was mainly due to different sizes of tissue preparations. Finally, the data set of ion dependencies consisted of 106 data points ($M = 106$ in Eq. 7), shown in Fig. 3 *A* and Fig. 4, *A* and *B*, which include a few invisible points. To calculate χ^2, all variables in Eq. 1 and SD were

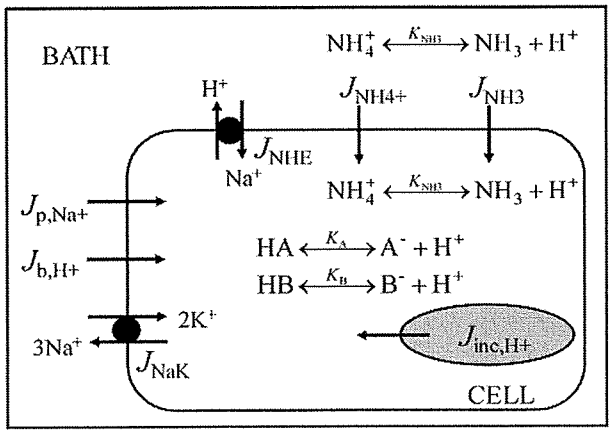

FIGURE 2 Simple cell model of cardiac Purkinje fibers. Abbreviations: $J_{p,Na+}$, passive flux of Na^+; $J_{b,H+}$, background H^+ flux; J_{NHE}, H^+ efflux or Na^+ influx through NHE; J_{NaK}, Na^+ efflux through the Na^+/K^+ pump; J_{NH3} and J_{NH4+}, passive fluxes of NH_3 and NH_4^+; and $J_{inc,H+}$, extra flux for intracellular H^+ increase by an unknown mechanism, which appears in Fig. 7. A^-, B^-, HA, and HB, free or H^+-bounded forms of intrinsic buffer species, A and B.

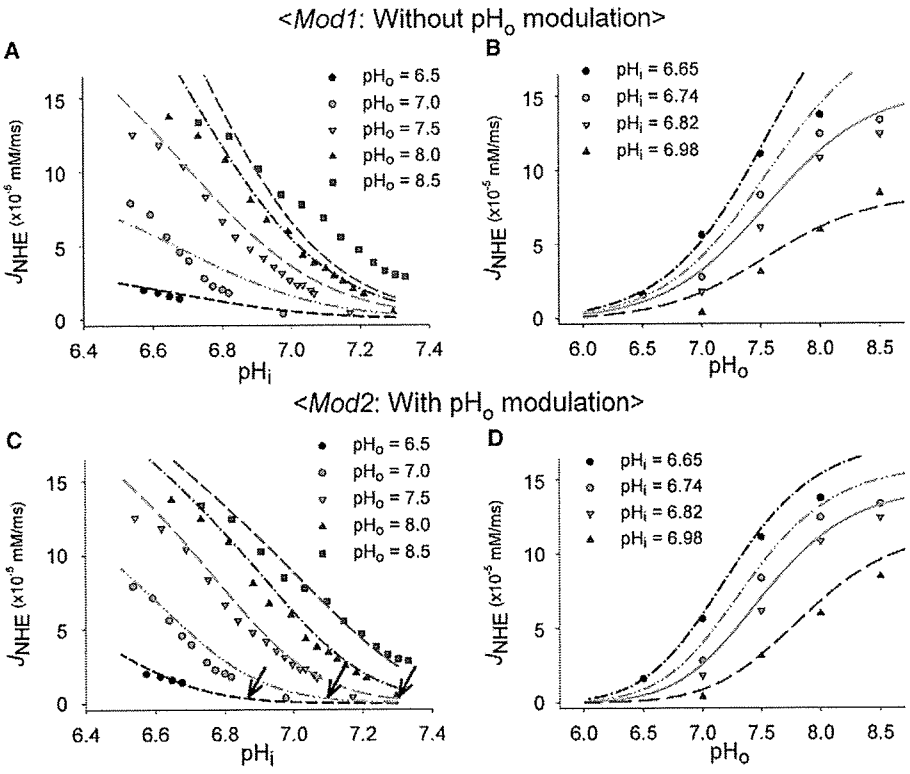

FIGURE 3 Comparison between *Mod1* and *Mod2* in response to pH_o variation. Experimental data (*symbols*) were taken from Vaughan-Jones and Wu (21). Various curves were plotted with the best fitting results for *Mod1* (*A* and *B*) or *Mod2* (*C* and *D*). Data points in panels *B* or *D* were selected from those in panels *A* or *C* for corresponding pH_i and pH_o, respectively. The arrows in panel *C* were fitted by eye to denote the location of each activation foot in the pH_i-NHE relationship at pH_o = 6.5, 7.0, and 7.5, respectively. Although data points were fitted with different $[Na^+]_i$, an average $[Na^+]_i$ was used to draw a continuous curve. This approximation may be justified, as the $[Na^+]_i$-J_{NHE} relation is shallow.

required, but $[Na^+]_i$ or SD was not always given in the literature. Therefore, $[Na^+]_i$ was supplemented from preliminary whole-cell simulations, and the ratio between SD and the mean of J_{NHE} described in the literature (25,30) was used for obtaining SD.

The forward/reverse mode of exchange was investigated in NHE1-transfected cells by measuring $^{22}Na^+$ flux (15). The forward mode offered information about the saturation of NHE activity at acidic pH_i below 5.2. The reverse mode provided important evidence that NHE includes a proton-

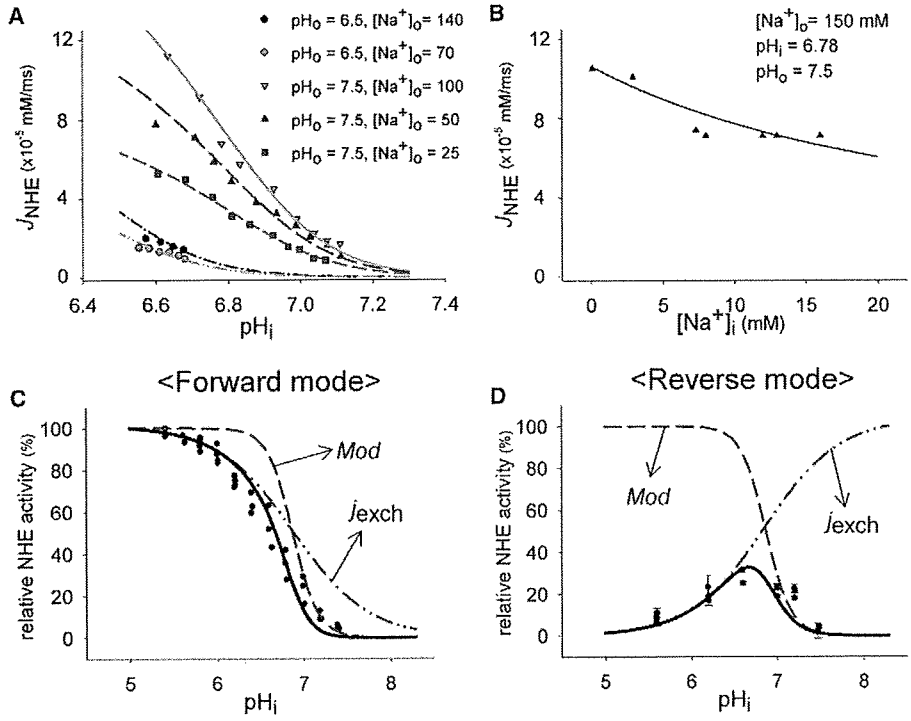

FIGURE 4 Best-fit results for NHE activity with *Mod2*. The data points in panels *A* and *B* (*symbols*) were taken from Wu and Vaughan-Jones (22). (*A*) pH_i-NHE relationship at various $[Na^+]_o$ and pH_o. As with Fig. 3, an average $[Na^+]_i$ was used to draw a continuous curve. (*B*) $[Na^+]_i$-NHE relationship. (*C* and *D*) The activities in the forward/reverse mode were simulated for $[Na^+]_i$ /$[Na^+]_o$ = 0 / 1 or 1 / 0 mM, based on the experimental studies (15). The J_{NHE} curves (*bold lines*) were determined from the product of j_{exch} and *Mod* (Eq. 1).

modifier part in addition to ion-exchanging part, and helped us to determine j_{exch} and *Mod* separately. The turnover rate was measured by dividing J_{NHE} by total number of NHE molecules in experiments (31,32), which correspond to (*Mod* × j_{exch}) in Eq. 1. The turnover rate of one NHE1 molecule is 2–10 ms^{-1} at pH_i = 6.0, pH_o = 7.4, $[Na^+]_i$ ~0, and $[Na^+]_o$ = 140 mM. We restricted this value to 2.3–2.5 ms^{-1} to avoid redundancies in the fitting results due to the inverse relationship between N and k values (refer to Eqs. 1–3).

Construction of a simple cell model

When pH_i recovers from acidification, $[Na^+]_i$ concurrently increases due to Na^+ influx through NHE. To check whether the experimental increase of $[Na^+]_i$ during pH_i recovery is attributable to the NHE activity, we incorporated the new NHE model into a simple cell model including the minimum components involved in pH_i or $[Na^+]_i$ regulation (Fig. 2). NBC and Cl^--HCO_3^- exchange were not considered because they are almost inactive in a HEPES-buffered system (1). A contribution of Cl^--OH^- exchange was included in a passive H^+ flux.

The equations for individual components are presented in the Appendix. For intracellular pH buffer (Eqs. 22–25), two intrinsic buffering species, A and B, were assumed. The total concentration and dissociation constants of A and B were determined based on the measurement of intrinsic pH buffering power in Purkinje fibers (33) (see the Supporting Material). Passive Na^+ flux (Eq. 13) is expressed by a constant field equation. The pH_i drift in Fig. 5 and Fig. 6 *B* in the absence of external Na^+ might be attributed to a background H^+. This flux seems to be larger at lower pH_o or at higher pH_i, and reversed to efflux at excessive acidic pH_i (22). Although Cl^--OH^- exchange is the potential candidate for the background H^+ flux in the CO_2/HCO_3^- free conditions (34,35), other unknown mechanisms might participate. Equation 14 is used only to describe the pH_i drift of unknown nature to complete the model fitting, but is not related to biophysical mechanisms. The equation for the Na^+/K^+ pump (Eq. 15) was adopted from the Kyoto model (36). We described flux of NH_4^+ with the constant field equation (Eq. 16) under the assumption that NH_4^+ is mainly transported through inwardly rectifying K^+ channels in cardiac myocytes (37). The NH_4^+ flux through Na^+/K^+ pump (38) or NHE (12) is neglected here, because the speed of acidification during NH_4Cl pulse is almost identical irrespective of the existence of Na^+ ion in intra-/extracellular medium (Fig. 5), which might affect NH_4^+ transport through Na^+/K^+ pump or NHE. Flux of NH_3 (Eq. 17) was expressed with Fick's law. The $[K^+]_i$ was set to be constant, assuming that K^+ permeability was dominant over others. For the same reason, the membrane potential was fixed at the K^+ equilibrium potential. This approximation is justified, since changes in the flux of Na^+ or NH_4^+ were small when the membrane potential was altered by $< \pm 10$ mV around the resting potential. The extracellular ionic composition was the same as that used in the experimental studies.

RESULTS

Determination of the NHE model scheme and parameters

The least χ^2 for the 16 model schemes were compared for different n_H values (see Table S2). Relatively large values were obtained with n_H = 1 for both *Mod1* and *Mod2*. However, it was difficult to determine which among n_H = 2, 3, and 4 was appropriate because of the marginal differences in χ^2. For the same reason, the six- and eight-state models of j_{exch} could not be differentiated.

A more careful approach than simple comparison of χ^2 was required to discriminate *Mod1* and *Mod2* because these

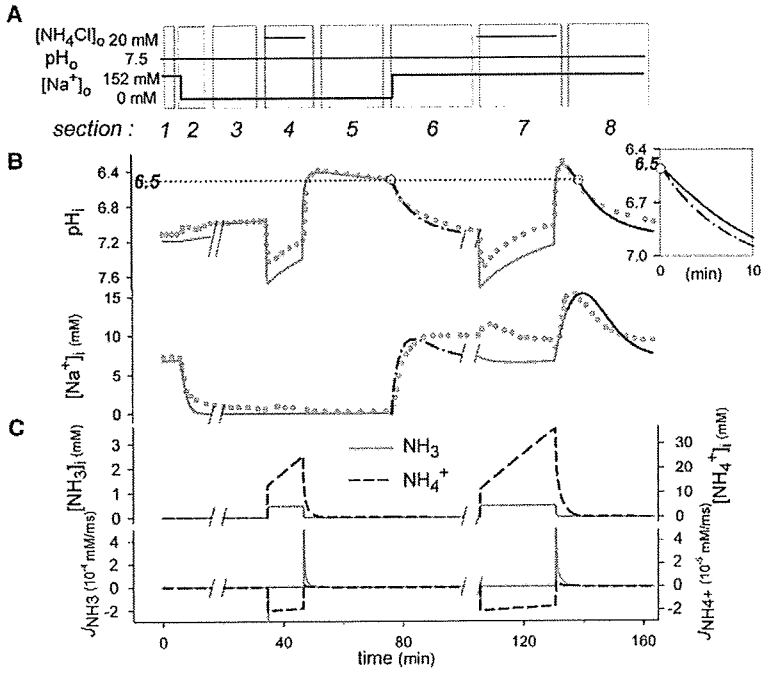

FIGURE 5 Simulation of pH_i and $[Na^+]_i$ variations in an NH_4Cl prepulse experiment. The original experimental recordings were from Fig. 5 in Wu and Vaughan-Jones (22). (*A*) The experimental protocol. (*B*) Changes of pH_i and $[Na^+]_i$ in the experiment (*shaded dots*) and in simulation (*lines*). (*Inset*) Comparison of the two recovery speeds at pH_i 6.5 between sections 6 and 8 in the simulation. Open circles indicate the time of comparison, which is indicated by a horizontal dotted line. The slash (*//*) denotes interruption of the simulation. (*C*) Simulated changes of $[NH_3]_i$, $[NH_4^+]_i$, J_{NH3}, and J_{NH4+}. ***Simulation of the response to an NH_4Cl prepulse***: The initial alkaline shift of pH_i was due to the almost instantaneous redistribution of NH_3 and the following relaxation is attributable to delayed accumulation of NH_4^+ within the cell. The subsequent sudden drop to pH_i 6.5 after removal of NH_4Cl was driven by the immediate and large efflux of NH_3. ***Determination of parameters for the cell model***: Cellular parameters were uniquely determined from the appropriate sections. $J_{b,H+}$ (Eq. 14) was determined from the slope of the pH change in sections 3 and 5, in which the other components were inactive due to the absence of Na^+. The amplitude of J_{NHE} (N) was determined by the recovery rate of pH_i in sections 8, where variation of $[Na^+]_i$ above 8 mM has little effect on NHE activity (22). J_{NaK} (D in Eq. 15) and $J_{p,Na+}$ (P_{Na+} in Eq. 13) were evaluated from the variations of $[Na^+]_i$ in sections 1 and 2. The parameters of J_{NH3} and J_{NH4+} (P_{NH3}, P_{NH4+} in Eqs. 16 and 17) were derived from section 4. P_{NH3} was determined by fitting the initial rising and final falling phase of pH_i record during NH_4Cl pulse, and P_{NH4+} from the slow acidification during the pulse and the rebound at the end of the pulse. P_{NH3} and P_{NH4+} had values comparable to those in previous simulation studies (46,47), if converted with a usual surface/volume ratio (36). The acid dissociation constant of NH_3/NH_4^+ (K_{NH3}) is 7.08 × 10^{-7} mM. We failed to avoid the small deviation of pH_i during NH_4Cl pulse when this common K_{NH3} was used for intracellular and extracellular medium. The values of model components are given in Table S3.

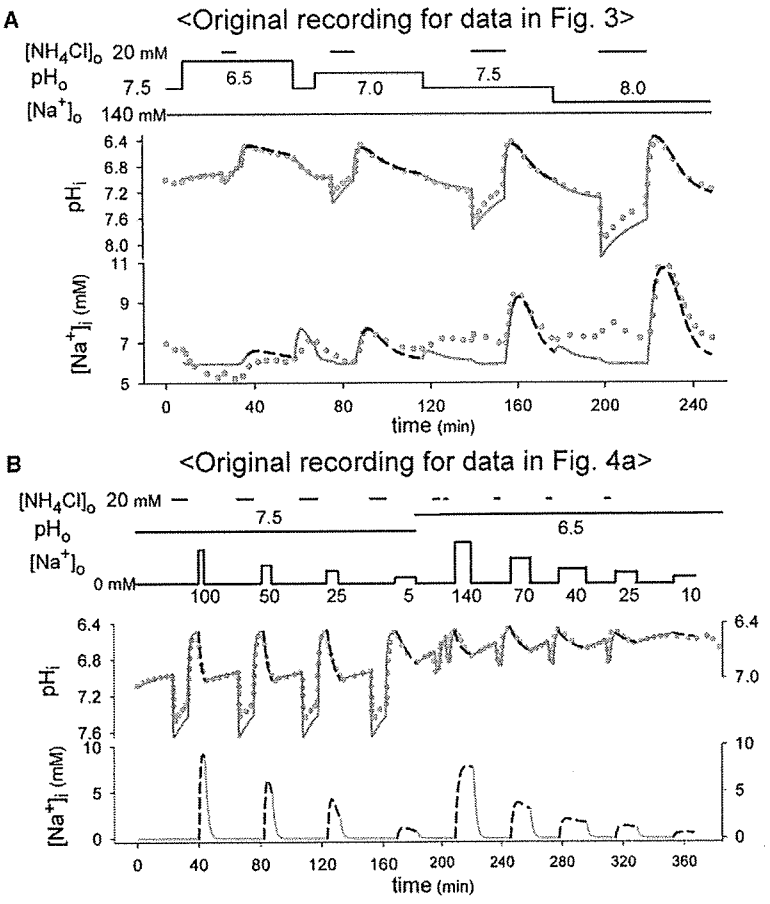

FIGURE 6 Simulations in various pH_o and $[Na^+]_o$. The experimental points (*shaded dots*) in panel *A* are from Fig. 6 in Vaughan-Jones and Wu (21) and those in panel *B* are from Fig. 1 in Wu and Vaughan-Jones (22). Dashed lines are simulated changes of pH_i and $[Na^+]_i$ in recovery periods from acidification. The values of model parameters were determined in a similar way to that in Fig. 5, except that N was already determined in the fitting procedure. In panel *B*, the parameters for J_{NaK} and $J_{p,Na+}$ determined in Fig. 5 were used, since $[Na^+]_i$ was not recorded in the original experiment. The values of model components are given in Table S3.

models had different numbers of unknown parameters. We found that the two models behaved differently in pH_o-induced inhibition (Fig. 3). *Mod2* could reconstruct the parallel shift of the pH_i-J_{NHE} relationship; that is, the activation foot moved to lower pH_i with decreasing pH_o (*arrows* in Fig. 3 *C*). Moreover, the pH_o-J_{NHE} relationship showed a clear saturation with increasing pH_o in agreement with experimental data (Fig. 3 *D*). In contrast, all the best-fit schemes of *Mod1* showed only scaling down in the NHE activity and failed to reconstruct the parallel shift of the pH_i-J_{NHE} and saturation by pH_o (Fig. 3, *A* and *B*). Therefore, we chose *Mod2* for characterizing the modulation by pH_o, which is in accord with the extracellular allosteric regulation suggested by Vaughan-Jones and Wu (21) and Vaughan-Jones and Spitzer (39).

Among the six plausible schemes for *Mod2*, we adopted the model using $n_H = 3$ with the eight-state ion-exchanging for the following simulations, simply because this model had the least χ^2, regardless of whether the difference between this and the other models was significant. The final parameter set (presented in Table S1) successfully reconstructed the dependencies on pH_i, $[Na^+]_o$, and $[Na^+]_i$ (Fig. 4, *A* and *B*), as well as the forward/reverse mode of NHE (Fig. 4, *C* and *D*) (15). We found that in the forward mode, the activation foot is determined by *Mod*, whereas the saturation at lower pH_i is dependent on j_{exch}. The slope is largely determined by cooperative activation in *Mod* with $n_H = 3$. In the reverse mode, j_{exch} and *Mod* change in opposite directions and J_{NHE} becomes bell-shaped.

Reconstruction of variations of pH_i and $[Na^+]_i$ in experimental recordings

Increase in $[Na^+]_i$ in NH_4Cl prepulse experiments

Wu and Vaughan-Jones (22) elaborated the experimental protocol shown in Fig. 5 *A* to examine effects of varying $[Na^+]_i$ on J_{NHE}. As the cell recovered from acidification in sections 6 and 8 in simulation (as depicted in Fig. 5), the counter Na^+ influx through NHE increased $[Na^+]_i$ to levels comparable to those in the experiment (Fig. 5 *B*). In both experiment and simulation, the range of $[Na^+]_i$ variation in section 6 was lower than that in section 8, and the initial rate of pH_i recovery was faster in section 6 (*inset* in Fig. 5). Since the simulation revealed that NH_3 and NH_4^+ were completely washed-out at $pH_i = 6.5$ (Fig. 5 *C*), it excluded the possibility that the remaining acid loading might retard recovery (an error factor mentioned in (21)). Thus, the

simulation results support the conclusion of Wu and Vaughan-Jones (22) that the different recovery speeds were caused by the depressed NHE activity at higher $[Na^+]_i$. For parameters of the cell model as well as mechanisms of inducing acidification by the NH_4Cl pulse, see Fig. 5 legend.

It is essential to consider variations of $[Na^+]_i$ as well as pH_i in evaluating the magnitude of J_{NHE}. We simulated the original recordings for obtaining the data points in Fig. 3 and Fig. 4 *A*, in which pH_o and $[Na^+]_o$ were varied. In the experiment (Fig. 6 *A*) giving the data points in Fig. 3, the recording protocol was analogous to section 8 in Fig. 5 and $[Na^+]_i$ varied over the range from 6 to 10 mM in both experiment and simulation. From the $[Na^+]_i$-J_{NHE} relationship (Fig. 4 *B*), it is evident that the magnitude of J_{NHE} in Fig. 3 is hardly affected by variations of $[Na^+]_i$ above 6 mM. On the other hand, the experimental protocol for the data points in Fig. 4 *A* (Fig. 6 *B*) is similar to that in section 6 in Fig. 5, and $[Na^+]_i$ increased from virtually 0 to various peak levels during recovery from acidification. Therefore, the amplitude of J_{NHE} in Fig. 4 *A* was clearly modified by the $[Na^+]_i$ variation, and that was why we supplemented individual experimental points in Fig. 4 *A* with corresponding values of $[Na^+]_i$ obtained by simulations (mentioned as preliminary simulations in Methods). Taken together, these simulation results confirmed that our NHE model is applicable when extracellular conditions are changed.

Acidification induced indirectly by blocking the Na^+/K^+ pump

An increase in $[Na^+]_i$ has been suggested to mediate the intracellular acidification when the Na^+/K^+ pump is inhibited through two mechanisms:

1. A depression of NHE activity due to a decrease in the transmembrane Na^+ gradient (40).
2. An induction of intracellular acidification linked to an increase of $[Ca^{2+}]_i$ through depression of Na^+-Ca^{2+} exchanger (NCX) (41,42).

First, we examined the extent of acidification induced by attenuating J_{NHE} through increased $[Na^+]_i$ (*black line* in Fig. 7). When 50% of the Na^+/K^+ pump was inhibited by 10 μM strophanthidin ($K_D = 1.12 \times 10^{-5}$ M (43)), $[Na^+]_i$ rose rapidly toward a saturating level beyond 16 mM, in agreement with the experimental data. However, pH_i was only reduced by 0.05, which was much smaller than the experimental drop of ~0.3. Next, we tested the second mechanism, in which an extra H^+ increment ($j_{inc,H+}$) occurs through an increase in $[Ca^{2+}]_i$ (*red line* in Fig. 7) (41). If $[Ca^{2+}]_i$ is mainly equilibrated by NCX in cardiac myocytes, $[Ca^{2+}]_i$ is a function of $[Na^+]_i^3$, provided that $[Ca^{2+}]_o$ and $[Na^+]_o$ remain constant:

$$\frac{[Ca^+]_i}{[Ca^+]_o} = \left(\frac{[Na^+]_i}{[Na^+]_o}\right)^3 \exp\left(\frac{V_m F}{RT}\right) \quad (8)$$

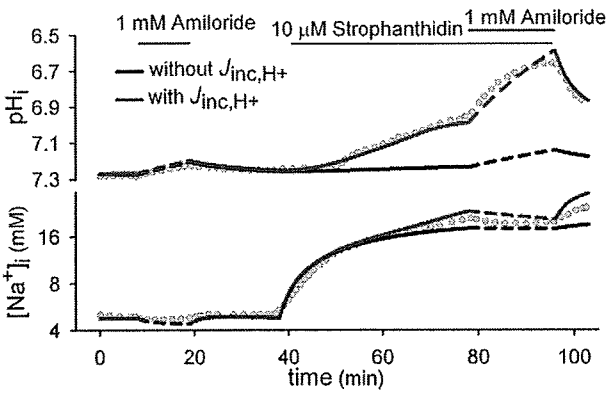

FIGURE 7 Effects of blocking the Na^+/K^+ pump on pH_i and $[Na^+]_i$. The original experimental recordings (*gray dots*) are taken from Fig. 2 in Kaila and Vaughan-Jones (42). Simulation results with (*red lines*) or without (*black lines*) an extra H^+ increment ($J_{inc,H+}$) are shown. Dashed lines indicate changes induced by applying amiloride. Most parameter values are the same as in Fig. 5, since the experimental conditions were comparable. The amplitudes of $J_{b,H+}$ and J_{NHE} were slightly modified to adjust the steady-state values of pH_i and $[Na^+]_i$ at time zero. The values of model components are given in Table S3.

(see Blaustein and Leder (44)). For simplicity, we assumed that $j_{inc,H+}$ is linearly proportional to $[Ca^{2+}]_i$ (or $[Na^+]_i^3$) within a limit (Eq. 18). In consequence, a decline of pH_i with an obvious delayed onset was obtained as in the experiment (see also (40)). In addition, the simulation successfully reconstructed the increased rate of acidification and the decrease of $[Na^+]_i$ during the complete blockage of NHE in the presence of strophanthidin in comparison to the control run. Although Eq. 18 is only a phenomenological description, the simulation supports the view that a Ca^{2+}-induced H^+ increment from an unknown origin contributes to acidification to a larger extent than depression of J_{NHE} through an increase in $[Na^+]_i$.

DISCUSSION

Here, for the first time to our knowledge, we have reconstructed the transient increase in $[Na^+]_i$ accompanying NHE activation at different $[Na^+]_o$ and pH_o. So far, there are two articles that offered simulated effects of acidosis on the developed tension with a cell model including electrical excitation, Ca^{2+} dynamics by the sarcoplasmic reticulum, contraction, and the modulation of various molecular functions at acidic pH_i (9,13). In contrast to those complicated simulations, we focused our simulations totally on the Purkinje fiber experiments, which recorded the time course of $[Na^+]_i$ variation caused by the NHE activation. For deeper understanding of regulation of $[Na^+]_i$ at different pH_i, we will discuss functional coupling between NHE and Na^+/K^+ pump during acidosis. We then determine the extent of $[Na^+]_i$ increase induced by acidosis using steady-state pH_i-$[Na^+]_i$ relationship, and discuss $[Na^+]_i$-J_{NHE} relationship by taking the thermodynamic driving force into account.

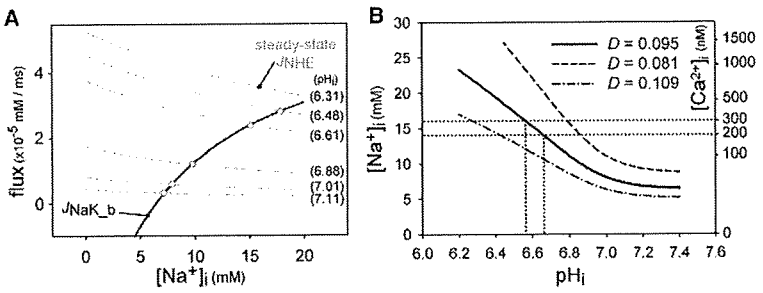

FIGURE 8 Steady-state relationship between pH_i and $[Na^+]_i$. (*A*) Na^+ flux balance between J_{NHE} and J_{NaK_b}. Gray curves indicate $[Na^+]_i$-J_{NHE} at the different pH_i values indicated on the right, and the black curve indicates J_{NaK_b}. Intersections of the J_{NHE} with J_{NaK_b} are marked with open circles. (*B*) The steady-state relationship between pH_i and $[Na^+]_i$, corresponding to intersections of the J_{NHE} and J_{NaK_b} in panel *A*. When the amplitude of the Na^+/K^+ pump was altered from $D = 0.095$ to $D = 0.081$ or 0.109, the curve shifted as indicated by the dashed lines. The steady-state $[Na^+]_i$ on the left axis was converted to $[Ca^{2+}]_i$ on the right axis using Eq. 8. The dotted lines indicate the critical levels of $[Na^+]_i$ and pH_i. The calculations were all conducted under the condition of a membrane potential of −52 mV, a reversal potential of K^+ at 20 mM $[K^+]_o$.

Relationship between acidosis and $[Na^+]_i$ or $[Ca^{2+}]_i$

The variation of $[Na^+]_i$ is determined by the balance among NHE, Na^+/K^+ pump, and passive Na^+ flux in our simple cell model. The time derivative of $[Na^+]_i$ is

$$\frac{d[Na^+]_i}{dt} = J_{NHE} - (J_{NaK} + J_{p,Na+})$$

(see Eq. 19). Since $[K^+]_o$ and the membrane potential are assumed to be constant, both J_{NaK} and $J_{p,Na+}$ are functions of only $[Na^+]_i$. To examine the major interaction between NHE and Na^+/K^+ pump, the sum of J_{NaK} and $J_{p,Na+}$ is treated as J_{NaK_b}, which is J_{NaK} biased by $J_{p,Na+}$ (Fig. 8 *A*). The intersections of the J_{NaK_b} and J_{NHE} curves correspond to $d[Na^+]_i/dt = 0$ and give steady-state values of $[Na^+]_i$ at each pH_i. This steady-state relationship is demonstrated by the continuous curve in Fig. 8 *B*. $[Na^+]_i$ is nearly constant on the alkaline side above pH_i 7.2 and increases linearly with acidosis. This Na^+ overload during persistent acidosis may affect cellular viability via a secondary $[Ca^{2+}]_i$ increment through NCX (45), which causes myocardial contracture. To investigate the critical level of acidosis, $[Na^+]_i$ is converted to $[Ca^{2+}]_i$ according to Eq. 8 (*right axis* in Fig. 8 *B*). Assuming that blood pumping of the ventricle is interfered with when diastolic $[Ca^{2+}]_i$ remains higher than the activation threshold of contraction at 200 or 300 nM, the critical $[Na^+]_i$ is 14–16 mM, or the critical pH_i is ~6.6. The critical pH_i moves in the acidic direction when J_{NaK} is depressed, and in the alkaline direction with enhanced J_{NaK} (*dotted lines* in Fig. 8 *B*). Similarly, the change in membrane leak conductance ($J_{p,Na+}$ in our model) under pathophysiological conditions may also affect the critical level of pH_i. To get a deeper insight into the critical level of acidosis, note that the pH sensitivity of channels, transporters, and contraction should also be accounted for in the model calculation in future.

Relationship between thermodynamic driving force and J_{NHE}

The variation of $[Na^+]_i$ affects the J_{NHE} via thermodynamic driving force, E_d, which is given as

$$E_d = RT \times \left(\ln\frac{[H^+]_i}{[H^+]_o} + \ln\frac{[Na^+]_o}{[Na^+]_i} \right). \quad (9)$$

With a constant pH_o/pH_i gradient and a fixed $[Na^+]_o$, E_d is a linear function of $\ln([Na^+]_i)$ and reverses its sign at an equilibrium value of $[Na^+]_i$ (Fig. 9 *A*). It should be noted that our model successfully defines the equilibrium value of $[Na^+]_i$ by adopting microscopic reversibility. Fig. 9 *A* indicates that the magnitude of J_{NHE} saturates below 3 mM $[Na^+]_i$ despite the linear increase of E_d. The dependency of J_{NHE} on E_d is given by the following equation, in analogy to Ohm's law,

$$J_{NHE} = gE_d, \quad (10)$$

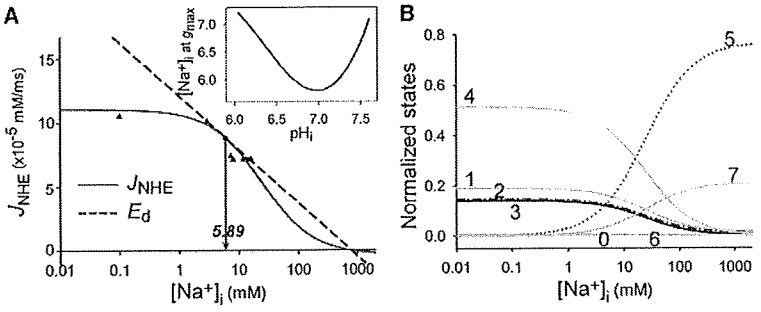

FIGURE 9 Variation of J_{NHE} and E_d, and transition of model states with $[Na^+]_i$. (*A*) The $[Na^+]_i$-J_{NHE} relationship (*solid line*) and E_d (*dashed line*) with a log scale for $[Na^+]_i$. J_{NHE} and data points (*triangles*) are identical, as shown in Fig. 4 *B*. E_d is zero at $[Na^+]_i = 787$ mM at $pH_i = 6.78$, $pH_o = 7.5$, and $[Na^+]_o = 150$ mM. (*Inset*) Point of tangency for g_{max} at each pH_i. (*B*) Distribution of states for the ion-exchanging part as a function of $[Na^+]_i$. Numerals indicate the states of NHE model, as defined in Fig. 1 *B*.

where g is the conductance of NHE (mol J^{-1} ms^{-1}) and is defined by the slope connecting each point on the J_{NHE} curve with the equilibrium point. The maximum g, g_{max}, appeared at $[Na^+]_i = 5.89$ mM, which is defined by a tangent line to the J_{NHE} at $pH_i = 6.78$. The values of $[Na^+]_i$ giving g_{max} were explored at various pH_i and are plotted against pH_i (*inset* of Fig. 9). It is evident that $[Na^+]_i$ at g_{max} remains in a narrow range over a wide range of pH_i; that is, the NHE model operates almost at g_{max} over the physiological range of $[Na^+]_i$, even during severe acidosis.

The $[Na^+]_i$ dependency of J_{NHE} or g is determined by the state distributions of the ion-exchanging part of the NHE model, as shown in Fig. 9 *B*:

$$J_{NHE} \propto (\text{state } 2)k_1^+ - (\text{state } 5)k_1^-. \tag{11}$$

When intracellular Na^+ is depleted, state 5, in which Na^+ binds on the intracellular side, becomes nearly 0. Accordingly, J_{NHE} is only dependent on state 2, thereby causing J_{NHE} to saturate. As $[Na^+]_i$ increases, states 5 and 7 accumulate at the expense of all the other states. An integrated effect of the variations of states 2 and 5 induces a gradual decay of g with increasing $[Na^+]_i$. Thus, the state rearrangement produces the sigmoidal dependency of J_{NHE} on $[Na^+]_i$ (Fig. 9 *A*).

APPENDIX

Equations for the simple cell model

$$CF_X = \frac{z_X F V_m}{RT} \frac{[X]_i - [X]_o \exp(-z_X F V_m/RT)}{1 - \exp(-z_X F V_m/RT)}, \text{ where } X = \{Na^+, NH_4^+\}. \tag{12}$$

$$J_{p,Na+} = P_{Na+} CF_{Na+}. \tag{13}$$

$$J_{b,H+} = A[H^+]_o + B\,pH_i + C. \tag{14}$$

$$J_{NaK} = D \frac{3 \times I_{NaK(\text{in kyoto model})}}{F\,vol_i}. \tag{15}$$

$$J_{NH4+} = P_{NH4+} CF_{NH4+}. \tag{16}$$

$$J_{NH3} = P_{NH3}([NH_3]_i - [NH_3]_o). \tag{17}$$

$$J_{inc,H+} = \begin{cases} E([Na^+]_i)^3 & (\text{when } J_{inc,H+} < Max_{inc,H+}) \\ Max_{inc,H+} & (\text{otherwise}) \end{cases}. \tag{18}$$

$$\frac{d[Na^+]_i}{dt} = J_{NHE} - J_{NaK} - J_{p,Na+}. \tag{19}$$

$$\frac{d([NH_3]_i + [NH_4^+]_i)}{dt} = -J_{NH3} - J_{NH4+}. \tag{20}$$

$$\frac{d([H^+]_i + [NH_4^+]_i + [HA]_i + [HB]_i)}{dt} = -J_{NHE} - J_{b,H+} - J_{NH4+} + J_{inc,H+}. \tag{21}$$

The following equilibrium reactions among NH_3, NH_4^+, H^+, and pH buffer A and B were calculated.

$$HA \overset{K_A}{\rightleftharpoons} A^- + H^+.$$

$$HB \overset{K_B}{\rightleftharpoons} B^- + H^+.$$

$$NH_4^+ \overset{K_{NH3}}{\rightleftharpoons} NH_3 + H^+.$$

$$[HA]_i + [A^-]_i = [TA]. \tag{22}$$

$$[HB]_i + [B^-]_i = [TB]. \tag{23}$$

$$K_A = \frac{[A^-]_i [H^+]_i}{[HA]_i}. \tag{24}$$

$$K_B = \frac{[B^-]_i [H^+]_i}{[HB]_i}. \tag{25}$$

$$K_{NH3} = \frac{[NH_3]_i [H^+]_i}{[NH_4^+]_i} = \frac{[NH_3]_o [H^+]_o}{[NH_4^+]_o}. \tag{26}$$

[TA] or [TB] is the total concentration of pH buffer of A or B, respectively. $[NH_3]_i$, $[NH_4^+]_i$, and $[H^+]_i$ were obtained by solving Eqs. 22–26 with the iteration method.

Definitions and values of the model parameters are given in Table S3.

SUPPORTING MATERIAL

One figure and three tables are available at http://www.biophysj.org/biophysj/supplemental/S0006-3495(09)01444-1.

The authors are grateful to Prof. T. Powell and colleagues in the Biosimulation projects of Kyoto University and Ritsumeikan University for continuous discussion during this study.

This work was supported by the Biomedical Cluster Kansai project of Ministry of Education, Culture, Sports, Science and Technology Japan.

REFERENCES

1. Leem, C. H., D. Lagadic-Gossmann, and R. D. Vaughan-Jones. 1999. Characterization of intracellular pH regulation in the guinea-pig ventricular myocyte. *J. Physiol.* 517:159–180.
2. Yamamoto, T., P. Swietach, A. Rossini, S. H. Loh, R. D. Vaughan-Jones, et al. 2005. Functional diversity of electrogenic Na^+-HCO_3^- cotransport in ventricular myocytes from rat, rabbit and guinea pig. *J. Physiol.* 562:455–475.
3. Vaughan-Jones, R. D., F. C. Villafuerte, P. Swietach, T. Yamamoto, A. Rossini, et al. 2006. pH-Regulated Na^+ influx into the mammalian ventricular myocyte: the relative role of Na^+-H^+ exchange and Na^+-HCO co-transport. *J. Cardiovasc. Electrophysiol.* 17 (Suppl 1):S134–S140.

4. ten Hove, M., J. G. van Emous, and C. J. van Echteld. 2003. Na^+ overload during ischemia and reperfusion in rat hearts: comparison of the Na^+/H^+ exchange blockers EIPA, cariporide and eniporide. *Mol. Cell. Biochem.* 250:47–54.
5. Hartmann, M., and U. K. Decking. 1999. Blocking Na^+-H^+ exchange by cariporide reduces Na^+-overload in ischemia and is cardioprotective. *J. Mol. Cell. Cardiol.* 31:1985–1995.
6. Kentish, J. C. 1999. A role for the sarcolemmal Na^+/H^+ exchanger in the slow force response to myocardial stretch. *Circ. Res.* 85:658–660.
7. Cingolani, H. E., N. G. Perez, E. A. Aiello, and M. C. de Hurtado. 2005. Intracellular signaling following myocardial stretch: an autocrine/paracrine loop. *Regul. Pept.* 128:211–220.
8. Crampin, E. J., N. P. Smith, A. E. Langham, R. H. Clayton, and C. H. Orchard. 2006. Acidosis in models of cardiac ventricular myocytes. *Philos. Transact. A Math. Phys. Eng. Sci.* 364:1171–1186.
9. Ch'en, F. F., R. D. Vaughan-Jones, K. Clarke, and D. Noble. 1998. Modeling myocardial ischemia and reperfusion. *Prog. Biophys. Mol. Biol.* 69:515–538.
10. Swietach, P., and R. D. Vaughan-Jones. 2005. Spatial regulation of intracellular pH in the ventricular myocyte. *Ann. N.Y. Acad. Sci.* 1047:271–282.
11. Alexander, R. T., A. Malevanets, A. M. Durkan, H. S. Kocinsky, P. S. Aronson, et al. 2007. Membrane curvature alters the activation kinetics of the epithelial Na^+/H^+ exchanger, NHE3. *J. Biol. Chem.* 282:7376–7384.
12. Weinstein, A. M. 1995. A kinetically defined Na^+/H^+ antiporter within a mathematical model of the rat proximal tubule. *J. Gen. Physiol.* 105:617–641.
13. Crampin, E. J., and N. P. Smith. 2006. A dynamic model of excitation-contraction coupling during acidosis in cardiac ventricular myocytes. *Biophys. J.* 90:3074–3090.
14. Niederer, S. A., and N. P. Smith. 2007. A mathematical model of the slow force response to stretch in rat ventricular myocytes. *Biophys. J.* 92:4030–4044.
15. Wakabayashi, S., T. Hisamitsu, T. Pang, and M. Shigekawa. 2003. Kinetic dissection of two distinct proton binding sites in Na^+/H^+ exchangers by measurement of reverse mode reaction. *J. Biol. Chem.* 278:43580–43585.
16. Moncoq, K., G. Kemp, X. Li, L. Fliegel, and H. S. Young. 2008. Dimeric structure of human Na^+/H^+ exchanger isoform 1 overproduced in *Saccharomyces cerevisiae*. *J. Biol. Chem.* 283:4145–4154.
17. Otsu, K., J. Kinsella, B. Sacktor, and J. P. Froehlich. 1989. Transient state kinetic evidence for an oligomer in the mechanism of Na^+-H^+ exchange. *Proc. Natl. Acad. Sci. USA.* 86:4818–4822.
18. Otsu, K., J. L. Kinsella, P. Heller, and J. P. Froehlich. 1993. Sodium dependence of the Na^+-H^+ exchanger in the pre-steady state. Implications for the exchange mechanism. *J. Biol. Chem.* 268:3184–3193.
19. Lacroix, J., M. Poet, C. Maehrel, and L. Counillon. 2004. A mechanism for the activation of the Na/H exchanger NHE-1 by cytoplasmic acidification and mitogens. *EMBO Rep.* 5:91–96.
20. Fuster, D., O. W. Moe, and D. W. Hilgemann. 2008. Steady-state function of the ubiquitous mammalian Na/H exchanger (NHE1) in relation to dimer coupling models with 2Na/2H stoichiometry. *J. Gen. Physiol.* 132:465–480.
21. Vaughan-Jones, R. D., and M. L. Wu. 1990. Extracellular H^+ inactivation of Na^+-H^+ exchange in the sheep cardiac Purkinje fiber. *J. Physiol.* 428:441–466.
22. Wu, M. L., and R. D. Vaughan-Jones. 1997. Interaction between Na^+ and H^+ ions on Na-H exchange in sheep cardiac Purkinje fibers. *J. Mol. Cell. Cardiol.* 29:1131–1140.
23. Aronson, P. S. 1985. Kinetic properties of the plasma membrane Na^+-H^+ exchanger. *Annu. Rev. Physiol.* 47:545–560.
24. Green, J., D. T. Yamaguchi, C. R. Kleeman, and S. Muallem. 1988. Cytosolic pH regulation in osteoblasts. Interaction of Na^+ and H^+ with the extracellular and intracellular faces of the Na^+/H^+ exchanger. *J. Gen. Physiol.* 92:239–261.
25. Wallert, M. A., and O. Frohlich. 1989. Na^+-H^+ exchange in isolated myocytes from adult rat heart. *Am. J. Physiol.* 257:C207–C213.
26. van Borren, M. M., A. Baartscheer, R. Wilders, and J. H. Ravesloot. 2004. NHE-1 and NBC during pseudo-ischemia/reperfusion in rabbit ventricular myocytes. *J. Mol. Cell. Cardiol.* 37:567–577.
27. Jean, T., C. Frelin, P. Vigne, P. Barbry, and M. Lazdunski. 1985. Biochemical properties of the Na^+/H^+ exchange system in rat brain synaptosomes. Interdependence of internal and external pH control of the exchange activity. *J. Biol. Chem.* 260:9678–9684.
28. Bountra, C., T. Powell, and R. D. Vaughan-Jones. 1990. Comparison of intracellular pH transients in single ventricular myocytes and isolated ventricular muscle of guinea-pig. *J. Physiol.* 424:343–365.
29. Petrecca, K., R. Atanasiu, S. Grinstein, J. Orlowski, and A. Shrier. 1999. Subcellular localization of the Na^+/H^+ exchanger NHE1 in rat myocardium. *Am. J. Physiol.* 276:H709–H717.
30. Hoffmann, G., Y. Ko, A. Sachinidis, B. O. Gobel, H. Vetter, et al. 1995. Kinetics of Na^+/H^+ exchange in vascular smooth muscle cells from WKY and SHR: effects of phorbol ester. *Am. J. Physiol.* 268:C14–C20.
31. Ng, L. L., J. E. Davies, M. Siczkowski, F. P. Sweeney, P. A. Quinn, et al. 1994. Abnormal Na^+/H^+ antiporter phenotype and turnover of immortalized lymphoblasts from type 1 diabetic patients with nephropathy. *J. Clin. Invest.* 93:2750–2757.
32. Siczkowski, M., J. E. Davies, and L. L. Ng. 1994. Activity and density of the Na^+/H^+ antiporter in normal and transformed human lymphocytes and fibroblasts. *Am. J. Physiol.* 267:C745–C752.
33. Vaughan-Jones, R. D., and M. L. Wu. 1990. pH dependence of intrinsic H^+ buffering power in the sheep cardiac Purkinje fiber. *J. Physiol.* 425:429–448.
34. Sun, B., C. H. Leem, and R. D. Vaughan-Jones. 1996. Novel chloride-dependent acid loader in the guinea-pig ventricular myocyte: part of a dual acid-loading mechanism. *J. Physiol.* 495:65–82.
35. Niederer, S. A., P. Swietach, D. A. Wilson, N. P. Smith, and R. D. Vaughan-Jones. 2008. Measuring and modeling chloride-hydroxyl exchange in the Guinea-pig ventricular myocyte. *Biophys. J.* 94:2385–2403.
36. Matsuoka, S., N. Sarai, S. Kuratomi, K. Ono, and A. Noma. 2003. Role of individual ionic current systems in ventricular cells hypothesized by a model study. *Jpn. J. Physiol.* 53:105–123.
37. Mitra, R. L., and M. Morad. 1991. Permeance of Cs^+ and Rb^+ through the inwardly rectifying K^+ channel in guinea pig ventricular myocytes. *J. Membr. Biol.* 122:33–42.
38. Bielen, F. V., H. G. Glitsch, and F. Verdonck. 1991. Dependence of Na^+ pump current on external monovalent cations and membrane potential in rabbit cardiac Purkinje cells. *J. Physiol.* 442:169–189.
39. Vaughan-Jones, R. D., and K. W. Spitzer. 2002. Role of bicarbonate in the regulation of intracellular pH in the mammalian ventricular myocyte. *Biochem. Cell Biol.* 80:579–596.
40. Deitmer, J. W., and D. Ellis. 1980. Interactions between the regulation of the intracellular pH and sodium activity of sheep cardiac Purkinje fibers. *J. Physiol.* 304:471–488.
41. Vaughan-Jones, R. D., W. J. Lederer, and D. A. Eisner. 1983. Ca^{2+} ions can affect intracellular pH in mammalian cardiac muscle. *Nature.* 301:522–524.
42. Kaila, K., and R. D. Vaughan-Jones. 1987. Influence of sodium-hydrogen exchange on intracellular pH, sodium and tension in sheep cardiac Purkinje fibers. *J. Physiol.* 390:93–118.
43. Levi, A. J. 1991. The effect of strophanthidin on action potential, calcium current and contraction in isolated guinea-pig ventricular myocytes. *J. Physiol.* 443:1–23.
44. Blaustein, M. P., and W. J. Lederer. 1999. Sodium/calcium exchange: its physiological implications. *Physiol. Rev.* 79:763–854.
45. Baartscheer, A. 2006. Chronic inhibition of Na^+/H^+-exchanger in the heart. *Curr. Vasc. Pharmacol.* 4:23–29.
46. Boron, W. F., and P. De Weer. 1976. Intracellular pH transients in squid giant axons caused by CO_2, NH_3, and metabolic inhibitors. *J. Gen. Physiol.* 67:91–112.
47. Benjelloun, F., N. Bakouh, J. Fritsch, P. Hulin, J. Lipecka, et al. 2005. Expression of the human erythroid Rh glycoprotein (RhAG) enhances both NH_3 and NH_4^+ transport in HeLa cells. *Pflugers Arch.* 450:155–167.

FEBS Letters 583 (2009) 3600–3604

ELSEVIER

FEBS Letters

journal homepage: www.FEBSLetters.org

Essential role of TRPV2 ion channel in the sensitivity of dystrophic muscle to eccentric contractions

Nadège Zanou [a], Yuko Iwata [b], Olivier Schakman [a], Jean Lebacq [a], Shigeo Wakabayashi [b], Philippe Gailly [a,*]

[a] Laboratory of Cell Physiology, Institute of Neurosciences, Université catholique de Louvain, 55/40 av. Hippocrate, 1200 Brussels, Belgium
[b] Department of Molecular Physiology, National Cardiovascular Center Research Institute Suita, Osaka 565-8565, Japan

ARTICLE INFO

Article history:
Received 4 September 2009
Revised 9 October 2009
Accepted 12 October 2009
Available online 17 October 2009

Edited by Gianni Cesareni

Keywords:
Eccentric contraction
Calcium
TRPV2
Duchenne muscular dystrophy

ABSTRACT

Duchenne myopathy is a lethal disease due to the absence of dystrophin, a cytoskeletal protein. Muscles from dystrophin-deficient mice (*mdx*) typically present an exaggerated susceptibility to eccentric work characterized by an important force drop and an increased membrane permeability consecutive to repeated lengthening contractions. The present study shows that mdx muscles are largely protected from eccentric work-induced damage by overexpressing a dominant negative mutant of TRPV2 ion channel. This observation points out the role of TRPV2 channel in the physiopathology of Duchenne muscular dystrophy.

1. Introduction

Duchenne muscular dystrophy (DMD) is a progressive neuromuscular disease affecting 1/3500 male birth (reviewed in [1,2]). It is characterized by an important muscle degeneration (foci of necrotic fibers) followed, at early stages, by an intense regeneration process. As the regenerative capacity diminishes, muscle tissue is progressively replaced by adipose and fibrous connective tissue, leading to an important muscle weakness. This pathology results from a mutation in the Xp21 locus, which leads to the lack of expression of dystrophin, a 427 kDa protein located at the cytoplasmic face of the sarcolemma [3,4]. In normal skeletal muscle cells, dystrophin is associated, at its carboxy-terminal domain, with a complex of transmembrane proteins constituted of β-dystroglycan and α-, β-, γ- and δ-sarcoglycans and called the dystrophin–glycoprotein complex (DGC [5,6]). The complex also binds to merosin (laminin-2), a component of the extracellular matrix. At its amino-terminal domain, dystrophin binds to cytoskeletal F-actin filaments (i.e. non-sarcomeric actin). Dystrophin thus constitutes a link between the cytoskeleton and the extracellular matrix [7]. The alteration of dystrophin expression has two main consequences: (i) it affects DGC targeting to the membrane and therefore causes a disruption of the link between the cytoskeleton and the extracellular matrix that could induce membrane fragility; (ii) it induces a disorganization of the cytoskeleton and leads to a disregulation of several ion channel types such as the acetylcholine receptor [8] and stretch-activated and stretch-inactivated channels [9–11]. The mechanism by which the absence of dystrophin leads to muscle fiber death remains partially unknown, but an abnormal entry of Ca^{2+} through membrane tears caused by the absence of dystrophin or through abnormally regulated channels seems to play a major role (reviewed in [12,13]). Indeed, in muscles from *mdx* mice, a genetic model of Duchenne muscular dystrophy, this abnormal entry of Ca^{2+} has been proved to activate several signaling cascades involved in cell damage such as Ca^{2+}-activated proteases (calpains) [14–16], phospholipase A_2 [17,18], accumulation of Ca^{2+} in the mitochondria [19] and production of ROS [20,21].

Recently, the involvement of a specific ion channel called TRPV2 in the pathophysiology of DMD was proposed [22]. TRPV2 protein belongs to the large family of TRP cationic channels involved in various processes of sensory signaling (sensing heat and cold, pH, osmolarity, etc. for review, see [23]). TRPV2 is activated by membrane stretch [24]. It normally localizes in the intracellular membrane compartments but translocates to the plasma membrane in dystrophic muscle fibers [25]. Its specific inhibition was shown to ameliorate muscular dystrophy. Indeed, *mdx* mice expressing a dominant negative mutant TRPV2 channel presented a reduced entry of Ca^{2+} in muscle fibers; as a consequence, they exhibited reduced muscle degeneration (necrosis and apoptosis) and regeneration (central nuclei, etc.). These observations suggest that TRPV2 channel constitutes the principal Ca^{2+} entry pathway in dystrophic muscle fibers.

* Corresponding author. Fax: +32 2 7645580.
E-mail address: philippe.gailly@uclouvain.be (P. Gailly).

0014-5793/$36.00 © 2009 Federation of European Biochemical Societies. Published by Elsevier B.V. All rights reserved.
doi:10.1016/j.febslet.2009.10.033

The most specific characteristic of dystrophic muscles is their particular sensitivity to eccentric (lengthening) contractions [26]. Indeed, repeated eccentric work of dystrophic muscles has been shown to induce a large and progressive loss of force as well as an important increase of membrane permeability which can be detected by the release of creatine kinase or by the uptake of membrane-impermeable dyes such as procion orange and Evans Blue dye. It is generally accepted that this is due to an abnormal fragility of the membrane, given the lack of connection between the cytoskeleton and the extracellular matrix. We tested an alternative hypothesis according to which muscle sensitivity to stretch would be primarily due to the abnormal presence at the plasma membrane or to the abnormal regulation of TRPV2 channels. We therefore studied eccentric contractions of EDL muscles from *mdx* mice expressing or not the dominant negative mutant of TRPV2. The progressive loss of force developed by muscles of these mice was very much reduced in comparison to *mdx* control mice, suggesting the involvement of TRPV2 channel in the increased sensitivity of dystrophic muscle to eccentric contractions. Interestingly, the uptake of procion orange dye was also significantly reduced, suggesting that the entry of Ca^{2+} through TRPV2 precedes the large increase of non-specific membrane permeability.

2. Materials and methods

2.1. Animals

Dystrophin-deficient C57BL/10ScSn-*DMD*^{mdx} (*mdx*) mice and their control C57 were from Jackson Laboratories. Generation of TRPV2 dominant negative (TRPV2-DN) transgenic mice (expressing the hemagglutinin (HA)-tagged E604 K mutant TRPV2 channel under the control of the α-skeletal actin promoter in skeletal muscle) has been described previously [22]. Male homozygous TRPV2-DN mice were mated with female *mdx* mice and the resulting male *mdx*/TRPV2-DN were analyzed.

All mice analyzed were 12–16 weeks of age. The experiments were approved by the Animal Ethics Committee of the Catholic University of Louvain, Brussels.

2.2. Muscle mechanical protocol

Mice were deeply anesthetized by intraperitoneal injection of a solution containing ketamine (10 mg ml^{-1}) and xylazine (1 mg ml^{-1}) in order to preserve muscle perfusion during dissection of extensor digitorum longus (EDL) and tibialis anterior muscles. Depth of anesthesia was assessed by the abolition of eyelid and pedal reflexes. After dissection, the animals were killed by cervical dislocation.

EDL muscles were bathed in a 1 ml horizontal chamber continuously superfused with HEPES buffered Krebs solution (100% O_2) containing (in mM): NaCl 135.5, KCl 5.9, $MgCl_2$ 1.2, $CaCl_2$ 2.5, HEPES sodium 11.6 and glucose 11.5, and maintained at a temperature of 20 ± 0.1 °C. One end of the muscle was tied to an isometric force transducer, and the other to an electromagnetic motor and length transducer. Stimulation (125 Hz) was delivered through platinum electrodes running in parallel to the muscles. Optimum muscle length (L_0) was carefully adjusted for maximal isometric force using 300 ms maximally fused tetani. Force was digitalized at a sampling rate of 1 kHz, using a PCI 6023E i/o card (National Instruments). Normalized stress was expressed relative to cross-sectional area, obtained by multiplying absolute force by the quotient "muscle fiber length (mm)/muscle blotted weight (mg)" and considering the fiber length equal to 0.5 × L_0 for EDL [27].

The muscles were subjected to a series of seven eccentric contractions consisting in 500 ms tetani during which a stretch of 1 mm (L_0 to L_0 + 8%) at a speed of 1 L_0 s^{-1} was applied 160 ms after the start of stimulation and maintained up to 250 ms after the start of stimulation (10 s interval between two successive tetani). Isometric force was measured for each tetanus just before the onset of the stretch and the percentage force drop was calculated.

2.3. Assessment of sarcolemmal damage

The stimulated muscle and its non-stimulated contralateral control were both bathed for 1 h in the oxygenated Krebs solution containing 1% procion orange. This dye is known to be excluded from intact cells but to penetrates damaged membranes [26,28]. The muscles were then rinsed twice in normal Krebs solution and were finally rapidly frozen in isopentane precooled with liquid N_2. Transverse 10 μm thick sections were cut from muscle midbelly region, mounted with vectashield solution and viewed in epifluorescence (Zeiss S100 inverted microscope, FITC filters). The area of procion orange positive fibers was measured as a percentage of the entire muscle cross-sectional area using ImageJ program (NCBI).

2.4. Reagents

The GsMTx4 toxin, isolated from *Grammostola spatulata* spider [29], was obtained from PeptaNova (Sandhausen, Germany); SFK-96365 (1-[B-[3-(4-methoxyphenyl)propoxy]-4-methoxyphenethyl]-1H-imidazole) from Alexis Corporation (Lausen, Switzerland)

2.5. Statistical analysis

Data are presented as means ± S.E.M. Unpaired *t*-tests were used to compare two groups and ANOVA to compare many groups. Significance level was fixed at $P < 0.05$.

3. Results

3.1. Dominant-negative inhibition of endogenous TRPV2 reduces the sensitivity of dystrophic muscle (mdx) to eccentric contractions

Isolated EDL muscles from *mdx* mice were submitted to successive eccentric contractions. We observed that dystrophin-deficient muscles presented a specific and progressive force drop (Fig. 1A and B). After six lengthening contractions, *mdx* muscles were able to develop less than 10% of the initial force; in the same conditions, their controls (C57) still developed 80% of the initial force. We and others previously reported that the channels abnormally activated in *mdx* fibers were sensitive to store depletion and membrane stretch [11,30,32]. In particular, we showed that they were sensitive to SKF-96365, a non-specific inhibitor of TRP channels [33] and to GsMTx4 toxin, the most specific inhibitor of mechanosensitive channels known today [29]. We therefore investigated the effect of these compounds on the sensitivity of *mdx* muscles to eccentric contractions. We observed that muscles incubated in the presence of 30 μM SKF-96365 (10 min preincubation) or in the presence of 10 μM GsMTx4 (2 h preincubation) developed significantly more force after a series of lengthening contractions than in the absence of the inhibitors (data not shown). These results confirm data reported by other groups using different eccentric contractions protocols [34] and suggest the involvement of these channels in the sensitivity to eccentric contractions. Since the best candidate of stretch-activated channel in skeletal muscle is TRPV2 [25], we studied the process on EDL muscles from normal C57 and dystrophic *mdx* mice expressing or not a dominant-negative mutant of TRPV2 (TRPV2-DN) [22]. We first observed that EDL muscles from *mdx* mice were bigger but developed less isometric

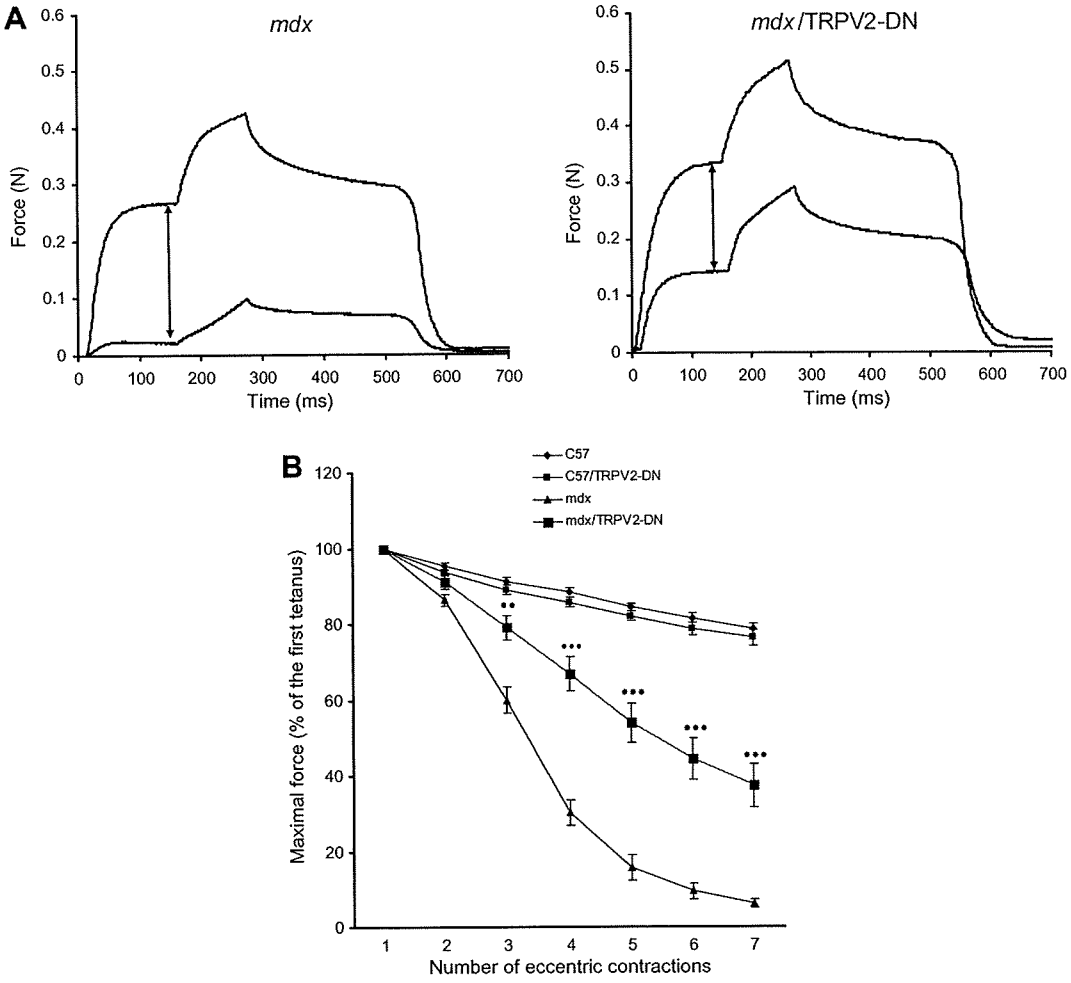

Fig. 1. Sensitivity to eccentric contractions. (A) Force traces of EDL muscle from *mdx* (left panel) and *mdx*/TRPV2-DN (right panel) mice. First and seventh tetanus presented. (B) Quantification of the force produced during repetitive eccentric contractions of EDL muscles from C57, C57/TRPV2, *mdx* and *mdx*/TRPV2. $^{**}P < 0.01$; $^{***}P < 0.001$ (one way repeated measures ANOVA, $n = 5–8$).

Table 1
Mechanicals properties of EDL muscles.

	C57	C57/TRPV2-DN	*mdx*	*mdx*/TRPV2-DN
Muscle weight (mg)	10.11 ± 0.22	9.84 ± 0.17	13.99 ± 0.49[a]	12.48 ± 0.31[a,b]
L_0 (mm)	11.75 ± 0.17	11.96 ± 0.26	11.82 ± 0.09	11.95 ± 0.09
F_0 (mN)	327.50 ± 32.88	358.46 ± 22.01	345.71 ± 21.87	330.73 ± 15.28
S_0 (mN/mm^2)	188.88 ± 16.93	219.23 ± 16.53	147.14 ± 9.85[a]	157.95 ± 3.98
n	5	8	8	6

[a] $P < 0.05$ vs C57.
[b] $P < 0.05$ vs *mdx*.

tension than controls (Table 1; Two way ANOVA, $P < 0.05$). This muscle pseudohypertrophy has been previously described in *mdx* mice [35]. Interestingly, in *mdx*/TRPV2-DN mice, EDL pseudohypertrophy was reduced (muscle weight significantly lower in *mdx*/TRPV2-DN than in *mdx*, and isometric tension slightly but not significantly higher in *mdx*/TRPV2-DN than in *mdx*, Table 1). When submitted to a series of eccentric contractions, EDL muscles from *mdx*/TRPV2-DN presented a much lower force drop than EDL from *mdx* mice (Fig. 1, one way repeated measures ANOVA, $P < 0.01–0.001$). The expression of TRPV2-DN had no effect on the force developed by C57 muscles during lengthening contractions.

These results strongly suggest a major role of TRPV2 channel in the stretch-induced force drop observed in *mdx* muscles.

3.3. Effect of dominant-negative inhibition of TRPV2 on stretch-induced membrane permeability in isolated muscles

To test whether the force drop in *mdx* muscle was correlated with the membrane permeability, isolated muscles were incubated for 1 h after a series of eccentric contractions in oxygenated Krebs solution containing 1% procion orange (a fluorescent dye substance which is excluded from intact cells but penetrate cells with membrane damage). Muscle cross-sections were analyzed for the percentage of procion orange positive fibers area related to the global area of the muscle section. As illustrated in Fig. 2, *mdx* muscles expressing the dominant negative mutant of TRPV2 presented a large reduction of the procion orange positive area compared to

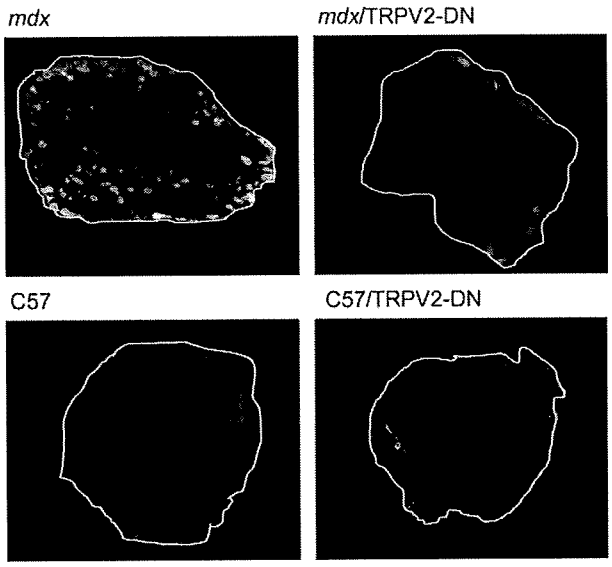

Fig. 2. Permeability to procion orange dye. Transverse sections of EDL muscles submitted to a series of seven lengthening contractions and then immersed during 1 h in procion orange containing Krebs solution. Sections examined under FITC fluorescence microscopy.

their *mdx* controls (11.46 ± 1.01% in *mdx*/TRPV2-DN vs 29.00 ± 3.72% in *mdx*, $n = 3$, $P < 0.05$). We checked that C57 and C57/TRPV2-DN muscles submitted to a series of eccentric contractions had a procion orange positive area that was always very low (below 5% of the total area) and limited to the periphery of muscles. Similarly, unstretched muscles (from C57, C57/TRPV2-DN, *mdx* and *mdx*/TRPV2-DN mouse strains) also present a negligible basal level of procion orange positive area.

4. Discussion

Since a long time, the importance of an abnormal influx of Ca^{2+} has been studied in skeletal myotubes from DMD patients [36] and in myotubes and adult fibers from *mdx* mice [14,37–40]. This influx has been shown to implicate various spontaneously active, store-dependent and/or mechanosensitive cationic channels [36,41] whereas the voltage-dependent Ca channels did not seem to be involved [41]. Accordingly, the channels involved were inhibited by lanthanides (Gd^{3+}, La^{3+}) and by pharmacological agents such as SKF-96365 and GsMTx4 toxin. We and others also showed that their occurrence at the membrane increased after myocyte stretch and after stimulation with IGF-1 [25,31,42], suggesting that they could be constituted of TRPV2 proteins [25,43,44]. This was clearly demonstrated recently. Indeed, transgenic or adenoviral expression of a dominant-negative TRPV2 in *mdx* muscles reduced several indices of the severity of the disease such as elevated serum creatine kinase level, number of apoptotic and necrotic fibers, intensity of the regeneration (central nuclei) and the consecutive fibrosis [22].

In the present study, we investigated the possible involvement of TRPV2 ion channel in the sensitivity of dystrophic muscle of *mdx* mice to eccentric contraction. This sensitivity constitutes the characteristic feature of the disease: forced lengthenings produce an important loss of force in dystrophic muscles [26,45]. This property is clearly related to membrane permeability and does not arise from factors within myofibrils [46]. Muscle fiber lesions resulting from eccentric contractions can be visualized by penetration of membrane-impermeant dyes like orange procion, suggesting that stretch of dystrophin-deficient membrane induces membrane tears, at least transiently [28]. Interestingly a linear relationship was observed between the percentage of orange procion positive fibers and the peak of tension observed at the end of eccentric contraction [45] and the force drop [47], suggesting that the high strain imposed on the fiber during forced lengthening produces localized disruptions of the plasma membrane that impairs mechanical response to electrical stimulation. However, the percentage of orange procion positive fibers was always smaller than the force drop (slope of relationship < 1). This was attributed to the fact that membrane lesions are localized; a single localized lesion completely prevents fiber contraction but as diffusion of the dyes is restricted, histochemical detection of these lesions could be under-estimated (few sections analyzed in a complete muscle) [2]. In this view, the increased fragility of the membrane due to the absence of dystrophin would explain the sensitivity of *mdx* muscles to eccentric contraction. However, this explanation was challenged by the observation that in muscles strained up to the point of membrane rupture, the absence of dystrophin had no detectable effect on the stress, the strain, or the energy absorbed, regardless of the state of muscle activation [48]. An alternative explanation was proposed by the group of Allen, who showed that short-term damage of *mdx* muscle fibers caused by stretch was partially prevented by blocking mechanosensitive channels [34,49]. This was confirmed here on isolated EDL muscles with a much milder protocol (8% stretch at $1\ L_0\ s^{-1}$ in our experiments vs 40% stretch at $4\ L_0\ s^{-1}$ in [49]). Interestingly, eccentric contractions also allowed an entry of Na^+ in *mdx* fibers through the same stretch-activated channels [50]. The prolonged increase of intracellular Na^+ concentration consecutive to eccentric contractions suggests that the loss of tension might be due, at least partially, not only to membrane damage but also to a prolonged membrane depolarization. This would explain the discrepancy between the percentage of damaged fibers (permeabilized to orange procion) and the amplitude of the force drop (see above). Here we compared the sensitivity to eccentric contractions in muscles from dystrophic mice expressing or not a dominant-negative TRPV2 channel. We show that muscles expressing the mutated channel are partially protected against eccentric contractions. Not only the force drop was very reduced, but the permeability to procion orange dye was significantly decreased, suggesting that the entry of ions through these channels precedes and is implicated in membrane lesions. This is in agreement with a recent study showing that reducing extracellular Ca^{2+} concentration or inhibiting calpain activity with leupeptin during lengthening contractions not only improved the force maintained but minimized membrane disruption [51]. This does not rule out an involvement of membrane fragility. Indeed, a significant force drop consecutive to repeated eccentric contractions is nevertheless still observed in dystrophic muscles expressing the dominant-negative TRPV2 mutant. Alternatively, this might be due to the fact that the entry of Ca^{2+} through native TRPV2 channels is not completely abolished in these muscles [22].

In conclusion, this study identifies TRPV2 as the mechanosensitive channel involved in eccentric work-induced force drop observed in dystrophic muscles. It suggests that the entry of cations, among which Ca^{2+}, through this channel is, at least partially, responsible for the observed membrane disruptions. Therefore, it constitutes a potentially interesting pharmacological target for the treatment of Duchenne muscular dystrophy.

Acknowledgements

We warmly thank M.L. Cao and M. Van Schoor for excellent technical assistance. We also acknowledge Dr. N. Tajeddine for helpful discussions. This work was supported by the "Association française contre les myopathies" (AFM), the "Association belge contre les maladies neuro-musculaires" (ABMM) and by a Grant

ARC 05/10-328 from the General Direction of Scientific Research of the French Community of Belgium.

References

[1] Blake, D.J., Weir, A., Newey, S.E. and Davies, K.E. (2002) Function and genetics of dystrophin and dystrophin-related proteins in muscle. Physiol. Rev. 82, 291–329.

[2] Gillis, J.M. (1999) Understanding dystrophinopathies: an inventory of the structural and functional consequences of the absence of dystrophin in muscles of the *mdx* mouse. J. Muscle Res. Cell Motil. 20, 605–625.

[3] Monaco, A.P., Neve, R.L., Colletti-Feener, C., Bertelson, C.J., Kurnit, D.M. and Kunkel, L.M. (1986) Isolation of candidate cDNAs for portions of the Duchenne muscular dystrophy gene. Nature 323, 646–650.

[4] Hoffman, E.P., Brown Jr., R.H. and Kunkel, L.M. (1987) Dystrophin: the protein product of the Duchenne muscular dystrophy locus. Cell 51, 919–928.

[5] Ervasti, J.M. and Campbell, K.P. (1991) Membrane organization of the dystrophin–glycoprotein complex. Cell 66, 1121–1131.

[6] Culligan, K.G., Mackey, A.J., Finn, D.M., Maguire, P.B. and Ohlendieck, K. (1998) Role of dystrophin isoforms and associated proteins in muscular dystrophy. Int. J. Mol. Med. 2, 639–648.

[7] Ervasti, J.M. and Campbell, K.P. (1993) A role for the dystrophin–glycoprotein complex as a transmembrane linker between laminin and actin. J. Cell Biol. 122, 809–823.

[8] Carlson, C.G. (1996) Acetylcholine receptor and calcium leakage activity in nondystrophic and dystrophic myotubes (MDX). Muscle Nerve 19, 1258–1267.

[9] Haws, C.M. and Lansman, J.B. (1991) Developmental regulation of mechanosensitive calcium channels in skeletal muscle from normal and *mdx* mice. Proc. Biol. Sci. 245, 173–177.

[10] Franco Jr., A. and Lansman, J.B. (1990) Calcium entry through stretch-inactivated ion channels in *mdx* myotubes. Nature 344, 670–673.

[11] Franco-Obregon Jr., A. and Lansman, J.B. (1994) Mechanosensitive ion channels in skeletal muscle from normal and dystrophic mice. J. Physiol. 481, 299–309.

[12] Ruegg, U.T. and Gillis, J.M. (1999) Calcium homeostasis in dystrophic muscle. Trends Pharmacol. Sci. 20, 351–352.

[13] Gailly, P. (2002) New aspects of calcium signaling in skeletal muscle cells: implications in Duchenne muscular dystrophy. Biochim. Biophys. Acta 1600, 38–44.

[14] Turner, P.R., Westwood, T., Regen, C.M. and Steinhardt, R.A. (1988) Increased protein degradation results from elevated free calcium levels found in muscle from *mdx* mice. Nature 335, 735–738.

[15] Badalamente, M.A. and Stracher, A. (2000) Delay of muscle degeneration and necrosis in *mdx* mice by calpain inhibition. Muscle Nerve 23, 106–111.

[16] Gailly, P., De Backer, F., Van Schoor, M. and Gillis, J.M. (2007) In situ measurements of calpain activity in isolated muscle fibres from normal and dystrophin-lacking *mdx* mice. J. Physiol. 582, 1261–1275.

[17] Iyer, S.L., Katyare, S.S. and Howland, J.L. (1976) Elevated erythrocyte phospholipase A associated with Duchenne and myotonic muscular dystrophy. Neurosci. Lett. 2, 103–106.

[18] Boittin, F.X., Petermann, O., Hirn, C., Mittaud, P., Dorchies, O.M., Roulet, E. and Ruegg, U.T. (2006) Ca^{2+}-independent phospholipase A_2 enhances store-operated Ca^{2+} entry in dystrophic skeletal muscle fibers. J. Cell Sci. 119, 3733–3742.

[19] Vandebrouck, A. et al. (2006) Regulation of store-operated calcium entries and mitochondrial uptake by minidystrophin expression in cultured myotubes. FASEB J. 20, 136–138.

[20] Ragusa, R.J., Chow, C.K. and Porter, J.D. (1997) Oxidative stress as a potential pathogenic mechanism in an animal model of Duchenne muscular dystrophy. Neuromuscul. Disord. 7, 379–386.

[21] Shkryl, V.M., Martins, A.S., Ullrich, N.D., Nowycky, M.C., Niggli, E. and Shirokova, N. (2009) Reciprocal amplification of ROS and Ca^{2+} signals in stressed *mdx* dystrophic skeletal muscle fibers. Pflugers Arch. 458, 915–928.

[22] Iwata, Y., Katanosaka, Y., Arai, Y., Shigekawa, M. and Wakabayashi, S. (2009) Dominant-negative inhibition of Ca^{2+} influx via TRPV2 ameliorates muscular dystrophy in animal models. Hum. Mol. Genet. 18, 824–834.

[23] Damann, N., Voets, T. and Nilius, B. (2008) TRPs in our senses. Curr. Biol. 18, R880–R889.

[24] Muraki, K., Iwata, Y., Katanosaka, Y., Ito, T., Ohya, S., Shigekawa, M. and Imaizumi, Y. (2003) TRPV2 is a component of osmotically sensitive cation channels in murine aortic myocytes. Circ. Res. 93, 829–838.

[25] Iwata, Y., Katanosaka, Y., Arai, Y., Komamura, K., Miyatake, K. and Shigekawa, M. (2003) A novel mechanism of myocyte degeneration involving the Ca^{2+}-permeable growth factor-regulated channel. J. Cell Biol. 161, 957–967.

[26] Moens, P., Baatsen, P.H. and Marechal, G. (1993) Increased susceptibility of EDL muscles from *mdx* mice to damage induced by contractions with stretch. J. Muscle Res. Cell Motil. 14, 446–451.

[27] Brooks, S.V. and Faulkner, J.A. (1988) Contractile properties of skeletal muscles from young, adult and aged mice. J. Physiol. 404, 71–82.

[28] Bansal, D., Miyake, K., Vogel, S.S., Groh, S., Chen, C.C., Williamson, R., McNeil, P.L. and Campbell, K.P. (2003) Defective membrane repair in dysferlin-deficient muscular dystrophy. Nature 423, 168–172.

[29] Suchyna, T.M., Johnson, J.H., Hamer, K., Leykam, J.F., Gage, D.A., Clemo, H.F., Baumgarten, C.M. and Sachs, F. (2000) Identification of a peptide toxin from *Grammostola spatulata* spider venom that blocks cation-selective stretch-activated channels. J. Gen. Physiol. 115, 583–598.

[30] Vandebrouck, C., Martin, D., Colson-Van Schoor, M., Debaix, H. and Gailly, P. (2002) Involvement of TRPC in the abnormal calcium influx observed in dystrophic (*mdx*) mouse skeletal muscle fibers. J. Cell Biol. 158, 1089–1096.

[31] Ducret, T., Vandebrouck, C., Cao, M.L., Lebacq, J. and Gailly, P. (2006) Functional role of store-operated and stretch-activated channels in murine adult skeletal muscle fibres. J. Physiol. 575, 913–924.

[32] Suchyna, T.M. and Sachs, F. (2007) Mechanosensitive channel properties and membrane mechanics in mouse dystrophic myotubes. J. Physiol. 581, 369–387.

[33] Putney, J.W. (2001) The pharmacology of capacitative calcium entry. Mol. Interventions 1, 84–94.

[34] Yeung, E.W., Whitehead, N.P., Suchyna, T.M., Gottlieb, P.A., Sachs, F. and Allen, D.G. (2005) Effects of stretch-activated channel blockers on $[Ca^{2+}]_i$ and muscle damage in the *mdx* mouse. J. Physiol. 562, 367–380.

[35] Lynch, G.S., Hinkle, R.T., Chamberlain, J.S., Brooks, S.V. and Faulkner, J.A. (2001) Force and power output of fast and slow skeletal muscles from mdx mice 6–28 months old. J. Physiol. 535, 591–600.

[36] Imbert, N., Vandebrouck, C., Constantin, B., Duport, G., Guillou, C., Cognard, C. and Raymond, G. (1996) Hypoosmotic shocks induce elevation of resting calcium level in Duchenne muscular dystrophy myotubes contracting in vitro. Neuromuscul. Disord. 6, 351–360.

[37] Tutdibi, O., Brinkmeier, H., Rudel, R. and Fohr, K.J. (1999) Increased calcium entry into dystrophin-deficient muscle fibres of MDX and ADR-MDX mice is reduced by ion channel blockers. J. Physiol. 515 (Pt 3), 859–868.

[38] Mallouk, N. and Allard, B. (2000) Stretch-induced activation of Ca^{2+}-activated K^+ channels in mouse skeletal muscle fibers. Am. J. Physiol. Cell Physiol. 278, C473–C479.

[39] Gailly, P., Boland, B., Himpens, B., Casteels, R. and Gillis, J.M. (1993) Critical evaluation of cytosolic calcium determination in resting muscle fibres from normal and dystrophic (*mdx*) mice. Cell Calcium 14, 473–483.

[40] Gailly, P., Hermans, E., Octave, J.N. and Gillis, J.M. (1993) Specific increase of genetic expression of parvalbumin in fast skeletal muscles of *mdx* mice. FEBS Lett. 326, 272–274.

[41] Imbert, N., Vandebrouck, C., Duport, G., Raymond, G., Hassoni, A.A., Constantin, B., Cullen, M.J. and Cognard, C. (2001) Calcium currents and transients in co-cultured contracting normal and Duchenne muscular dystrophy human myotubes. J. Physiol. 534, 343–355.

[42] Rolland, J.F., De Luca, A., Burdi, R., Andreetta, F., Confalonieri, P. and Conte Camerino, D. (2006) Overactivity of exercise-sensitive cation channels and their impaired modulation by IGF-1 in *mdx* native muscle fibers: beneficial effect of pentoxifylline. Neurobiol. Dis. 24, 466–474.

[43] Kanzaki, M., Zhang, Y.Q., Mashima, H., Li, L., Shibata, H. and Kojima, I. (1999) Translocation of a calcium-permeable cation channel induced by insulin-like growth factor-I. Nat. Cell Biol. 1, 165–170.

[44] Kowase, T., Nakazato, Y., Yoko, O.H., Morikawa, A. and Kojima, I. (2002) Immunohistochemical localization of growth factor-regulated channel (GRC) in human tissues. Endocr. J. 49, 349–355.

[45] Petrof, B.J., Shrager, J.B., Stedman, H.H., Kelly, A.M. and Sweeney, H.L. (1993) Dystrophin protects the sarcolemma from stresses developed during muscle contraction. Proc. Natl. Acad. Sci. USA 90, 3710–3714.

[46] Lynch, G.S., Rafael, J.A., Chamberlain, J.S. and Faulkner, J.A. (2000) Contraction-induced injury to single permeabilized muscle fibers from *mdx*, transgenic *mdx*, and control mice. Am. J. Physiol. Cell Physiol. 279, C1290–C1294.

[47] Deconinck, N., Rafael, J.A., Beckers-Bleukx, G., Kahn, D., Deconinck, A.E., Davies, K.E. and Gillis, J.M. (1998) Consequences of the combined deficiency in dystrophin and utrophin on the mechanical properties and myosin composition of some limb and respiratory muscles of the mouse. Neuromuscul. Disord. 8, 362–370.

[48] Law, D.J., Caputo, A. and Tidball, J.G. (1995) Site and mechanics of failure in normal and dystrophin-deficient skeletal muscle. Muscle Nerve 18, 216–223.

[49] Yeung, E.W., Head, S.I. and Allen, D.G. (2003) Gadolinium reduces short-term stretch-induced muscle damage in isolated *mdx* mouse muscle fibres. J. Physiol. 552, 449–458.

[50] Yeung, E.W., Ballard, H.J., Bourreau, J.P. and Allen, D.G. (2003) Intracellular sodium in mammalian muscle fibers after eccentric contractions. J. Appl. Physiol. 94, 2475–2482.

[51] Zhang, B.T., Yeung, S.S., Allen, D.G., Qin, L. and Yeung, E.W. (2008) Role of the calcium-calpain pathway in cytoskeletal damage after eccentric contractions. J. Appl. Physiol. 105, 352–357.

X-ray Structure Analysis Online 2009, VOL. 25

X-ray Structure Analysis Online

Crystal Structure of Ganciclovir

Tomoko KAWAMURA and Noriaki HIRAYAMA†

Basic Medical Science and Molecular Medicine, Tokai University School of Medicine, 143 Shimokasuya, Isehara, Kanagawa 259-1193, Japan

The crystal of the title compound, $C_9H_{13}N_5O_4$, belongs to space group $P2_1$ with cell dimensions a = 4.380(2), b = 10.909(4), c = 11.601(4)Å, and β = 99.11(3)°. The final R value is 0.0583. The chain moiety corresponding to the ribose ring in guanosine does not adopt a fully extended conformation. The relative orientation of the purine ring and the ether oxygen atom is similar to that observed in one of the crystallographically independent guanosine molecules in the crystal structure of guanosine dehydrate.

(Received December 24, 2008; Accepted February 27, 2009; Published on web May 10, 2009)

Ganciclovir (9-((1,3-dihydroxypropan-2-yloxy)methyl)-2-amino-1*H*-purin-6(9*H*)-one) is an acyclic guanine nucleoside analog, which has inhibitory activity against all herpesviruses, but is especially active against cytomegalovirus (CMV).[1] Ganciclovir inhibits viral DNA synthesis. It is phosphorylated to a deoxyguanosine triphosphate (dGTP) analogue. This competitively inhibits the incorporation of dGTP by viral DNA polymerase, resulting in terminating the elongation of viral DNA. Ganciclovir is effective for the treatment and chronic suppression of CMV rerinitis in immunocompromised patients, and the prevention of CMV disease in transplant patients. Although Ganciclovir is widely used as an antiviral agent, the three-dimensional structure has not been determined so far. An X-ray analysis of the title compound was undertaken to disclose its inherent three-dimensional structure, which is essential for the development of better antiviral drugs.

Ganciclovir was purchased from Sigma. Single crystals of the molecule were grown from a dimethylformamide solution. Despite repeated crystallization, it was extremely difficult to obtain good single crystals. The biggest single crystal after many crystallization experiments was a colorless fine-needle crystal with a size of 0.3 × 0.01 × 0.01 mm. It was mounted on a glass fiber, and used for data collection. The structure was solved by direct methods, and non-H atoms were refined by a full-matrix least-squares method with anisotropic temperature factors. The positions of H-atoms of the amino and hydroxyl groups were obtained from Fourier syntheses. The positions of other H-atoms were geometrically calculated. H-atoms were not refined. An elongated thermal ellipsoid of C8 is indicative of disorder, but it was not possible to separate the disordered positions. The crystal and experimental data are given in Table 1.

The molecular structure, drawn by ORTEP-III,[4] is shown in Fig. 2. Selected bond lengths and bond angles are given in Table 2. The bond lengths and angles are within the expected ranges. The geometrical parameters in the purine ring do not differ significantly from the corresponding values in the guanosine molecules in the crystal structure of guanosine dihydrate.[5] The chain moiety corresponding to the ribose ring in guanosine does not adopt a fully extended conformation with the torsion angles of N4-C6-O2-C7, C6-O2-C7-C9 and O2-C7-

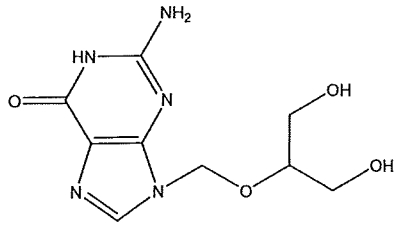

Fig. 1 Chemical structure of ganciclovir..

Table 1 Crystal and experimental data

Formula: $C_9H_{13}N_5O_4$	
Formula weight = 255.23	
Crystal system: monoclinic	
Space group: $P2_1$	Z = 2
a = 4.380(2)Å	
b = 10.909(4)Å	β = 99.11(3)°
c = 11.601(4)Å	
V = 547.3(3)Å^3	
D_x = 1.549 g/cm^3	
No. of observations (all) = 1713	
θ_{max} = 68.09° with Cu K_α	
R ($I > 2.00\sigma(I)$) = 0.0583	
Rw(all) = 0.0561	
$(\Delta/\sigma)_{max}$ = 0.005	
$(\Delta\rho)_{max}$ = 0.45 e/Å^3	
$(\Delta\rho)_{min}$ = –0.78 e/Å^3	
Measurement: Rigaku RAXIS-RAPID	
Program system: CrystalStructure 3.6.0[1]	
Structure determination: SIR92[2]	
Refinement: full-matrix	
CCDC deposition number: 714337	

† To whom correspondence should be addressed.
E-mail: hirayama@is.icc.u-tokai.ac.jp

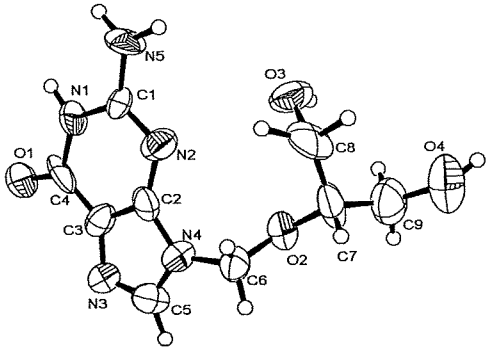

Fig. 2 Molecular structure of ganciclovir along with the labeling atoms. Thermal ellipsoids of non-H atoms are drawn at the 50% probability level.

Table 2 Selected bond lengths (Å), bond angles (°) and torsion angles (°)

O(1)—C(4)	1.25(1)	O(2)—C(6)	1.42(1)
O(2)—C(7)	1.45(1)	O(3)—C(8)	1.33(2)
O(4)—C(9)	1.45(2)	N(1)—C(1)	1.37(1)
N(1)—C(4)	1.38(2)	N(2)—C(1)	1.36(1)
N(2)—C(2)	1.35(2)	N(3)—C(3)	1.38(1)
N(3)—C(5)	1.31(2)	N(4)—C(2)	1.38(1)
N(4)—C(5)	1.36(1)	N(4)—C(6)	1.48(1)
N(5)—C(1)	1.35(1)		
C(7)—O(2)—C(6)	110.1(7)	C(4)—N(1)—C(1)	126.9(9)
C(2)—N(2)—C(1)	111.0(8)	C(5)—N(3)—C(3)	100.5(8)
C(5)—N(4)—C(2)	106.1(8)	C(6)—N(4)—C(2)	124.4(8)
C(6)—N(4)—C(5)	129.5(8)	N(1)—C(1)—N(2)	122.7(9)
N(1)—C(1)—N(5)	118.3(9)	N(2)—C(1)—N(5)	119.0(9)
N(2)—C(2)—N(4)	126.7(8)	N(2)—C(2)—C(3)	130(1)
N(4)—C(2)—C(3)	102.9(9)	N(3)—C(3)—C(2)	114.5(9)
N(3)—C(3)—C(4)	128.1(9)	O(1)—C(4)—N(1)	120(1)
O(1)—C(4)—C(3)	129(1)	N(1)—C(4)—C(3)	111.7(8)
N(3)—C(5)—N(4)	115.9(9)	O(2)—C(6)—N(4)	104.3(7)
O(2)—C(7)—C(8)	109.0(9)	O(2)—C(7)—C(9)	102.5(8)
O(3)—C(8)—C(7)	109(1)	O(4)—C(9)—C(7)	107.4(9)
C(7)—O(2)—C(6)—N(4)	152.7(7)	C(6)—O(2)—C(7)—C(8)	-77(1)
C(6)—O(2)—C(7)—C(9)	155.4(8)	C(4)—N(1)—C(1)—N(2)	-2(2)
C(4)—N(1)—C(1)—N(5)	178(1)	C(1)—N(1)—C(4)—O(1)	178(1)
C(1)—N(1)—C(4)—C(3)	1(2)	C(2)—N(2)—C(1)—N(1)	2(2)
C(2)—N(2)—C(1)—N(5)	-178(1)	C(1)—N(2)—C(2)—N(4)	179(1)
C(1)—N(2)—C(2)—C(3)	-2(2)	C(5)—N(3)—C(3)—C(2)	2(1)
C(5)—N(3)—C(3)—C(4)	179(1)	C(3)—N(3)—C(5)—N(4)	-1(1)
C(5)—N(4)—C(2)—N(2)	-179(1)	C(5)—N(4)—C(2)—C(3)	1(1)
C(6)—N(4)—C(2)—N(2)	2(2)	C(6)—N(4)—C(2)—C(3)	-177.5(9)
C(2)—N(4)—C(5)—N(3)	0(1)	C(6)—N(4)—C(5)—N(3)	179(1)
C(2)—N(4)—C(6)—O(2)	-71(1)	C(5)—N(4)—C(6)—O(2)	111(1)
N(2)—C(2)—C(3)—N(3)	179(1)	N(2)—C(2)—C(3)—C(4)	1(2)
N(4)—C(2)—C(3)—N(3)	-2(1)	N(4)—C(2)—C(3)—C(4)	-179.6(9)
N(3)—C(3)—C(4)—O(1)	6(2)	N(3)—C(3)—C(4)—N(1)	-178(1)
C(2)—C(3)—C(4)—O(1)	-177(1)	C(2)—C(3)—C(4)—N(1)	-1(2)
O(2)—C(7)—C(8)—O(3)	-63(2)	C(9)—C(7)—C(8)—O(3)	54(2)
O(2)—C(7)—C(9)—O(4)	-172.4(8)	C(8)—C(7)—C(9)—O(4)	67(1)

Table 3 Hydrogen bonds. D and A denote the hydrogen donor and acceptor, respectively.

D-H···A	D-H(Å)	H···A(Å)	D···A(Å)	D-H···A(°)
N1-H···N3$^{i)}$	0.96	1.90	2.84(1)	116
N5···O1$^{ii)}$	0.96	1.92	2.85(1)	162
N5···O4$^{ii)}$	0.97	2.28	3.09(1)	141
O4···O1$^{iii)}$	0.82	2.12	2.871(9)	151

Symmetry code: i) (–*x*, –1/2+*y*, –*z*); ii) (2–*x*, –1/2+*y*, 1–*z*); iii) (1+*x*, *y*, 1+*z*).

C9-O4 being 152.7(7), 155.4(8) and –172.4(8)°, respectively. The torsion angle of C2-N4-C6-O2, which determines the relative disposition of the purine ring and the ether oxygen atom, is –71(1)°. The corresponding angle in guanosine determines the relative orientation of the purine and ribose rings, and it is –137.2(8) and –58.1(7)° for crystallographically independent molecules in the crystal structure of guanosine dihydrate. It is interesting to note that the relative orientation of the base ring and the ether oxygen atom in ganciclovir is similar to that observed in one of the independent molecules of guanosine dihydrate. It is likely that the conformation is related to the biological activity of ganciclovir. There are four intermolecular hydrogen bonds, as given in Table 3.

Acknowledgements

This work was supported by Grants for the Key Technology Research Promotion Program of New Energy and Industrial Technology Development Organization (NEDO) of Japan, and also by the Research and Study Program of Tokai University Educational System General Research Organization.

References

1. S. Noble and D. Faulds, *Drugs*, **1998**, *56*, 115.
2. CrystalStructure, version 3.5.1, **2000 – 2003** Crystal Structure Analysis Package, Rigaku and Rigaku/MSC.
3. SIR92: A. Altomare, G. Cascarano, C. Giacovazzo, A. Guagliardi, M. Burla, G. Polidori, and M. Camalli, *J. Appl. Cryst.*, **1994**, *27*, 435.
4. ORTEP III, L. J. Farrugia, *J. Appl. Cryst.*, **1997**, *22*, 389.
5. U. Thewalt, C. E. Bugg, and R. E. Marsh, *Acta Crystallogr., Sect. B*, **1970**, *26*, 1089.

X-ray Structure Analysis Online 2009, VOL. 25

X-ray Structure Analysis Online

Crystal Structure of a Novel Diyne, 1,4-Bis(4-((Z)-1-phenyl-2-(trimethylsilyl)vinyl)phenyl)buta-1,3-diyne

Fumiaki ANZAI,* Takumi KATAISHI,* Taichi NAKANO,* Mieko HIRAYAMA, and Noriaki HIRAYAMA**†**

**Department of Materials Chemistry, School of High-Technology for Human Welfare, Tokai University, 317 Nishino, Numazu, Shizuoka 410-0395, Japan*

***Basic Medical Science and Molecular Medicine, Tokai University School of Medicine, 143 Shimokasuya, Isehara, Kanagawa 259-1143, Japan*

The crystal of the title compound, $C_{38}H_{38}Si_2$, belongs to space group $P\bar{1}$ with cell dimensions of a = 8.6324(6), b = 6.8543(5), c = 27.610(2)Å, α = 89.982(4), β = 89.783(4), and γ = 89.990(5)°. The final R value is 0.057. The central 1,4-diphenylbuta-1,3-diyne moiety takes a linear and planar structure. The trimethylsilyl and the terminal phenyl groups are located on opposite sides with respect to the central planar part.

(Received, October 23, 2008; Accepted March12, 2009; Published on web May 10, 2009)

Organic compounds possessing a high degree of conjugation such as phenylenes or phenyleneethynylenes have long been recognized as ideal materials for advanced electronics and photonic applications such as organic LEDs, liquid crystal displays, and solar cells.[1,2] During a research process of attempting to synthesize X-shaped phenyleneethynylene with terminal vinylsilane units, a novel diyne (1,4-bis(4-((Z)-1-phenyl-2-(trimethylsilyl)vinyl)phenyl)buta-1,3-diyne) was incidentally obtained by a reaction of (Z)-1-(4-ethenylphenyl)-1-phenyl-2-silylethene with 1,2,4,5-tetrabromobenzene. The chemical structure is shown in Fig. 1. An X-ray analysis was undertaken in order to disclose the inherent three-dimensional structure of this novel compound.

Single crystals were obtained from an ethyl acetate-hexane solution. A colorless platelet crystal with a size of 0.38 × 0.35 × 0.10 mm was mounted on a glass fiber and used for data collection. The structure was solved by direct methods and non-H atoms were refined by a full-matrix least-squares method with anisotropic temperature factors. The positions of all H-atoms were located by a difference Fourier synthesis and refined isotropically. The atomic parameters of the H-atoms were fixed in the final refinement. The crystal and experimental data are given in Table 1. The crystal structure shows a symmetry close to space group $P2_1/c$. However, the R_{int} value for the Laue symmetry $2/m$ was 0.042, which is significantly larger than 0.037 for the Laue symmetry $\bar{1}$. In addition, a refinement using space group $P2_1/c$ converged (Δ/σ = 0.000) at a relatively high R factor of 0.075. On the final difference Fourier map significant residual electron densities were observed with $(\Delta\rho)_{max}$ and $(\Delta\rho)_{min}$ being 0.75 and –0.82 e/Å^3, respectively. Therefore we lowered the crystal symmetry to $P\bar{1}$ and it helped with a successful structure refinement.

Two independent molecules located on the center of symmetry are present in an asymmetric unit. The molecular structure of one of the independent molecules, drawn by ORTEP-III, is shown in Fig. 2 with ring labelling. The molecules whose labels

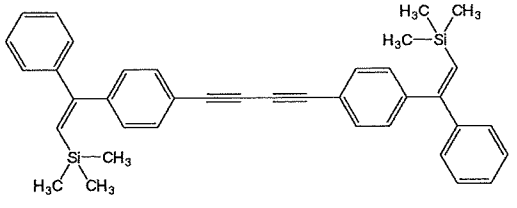

Fig. 1 Chemical structure of 1,4-bis(4-((Z)-1-phenyl-2-(trimethylsilyl)vinyl)phenyl)buta-1,3-diyne.

Table 1 Crystal and experimental data

Formula: $C_{38}H_{38}Si_2$	
Formula weight = 550.89	
Crystal system: triclinic	
Space group: $P\bar{1}$	Z = 2
a = 8.6324(6)Å	α = 89.982(4)°
b = 6.8543(5)Å	β = 89.783(4)°
c = 27.610(2)Å	γ = 89.990(5)°
V = 1633.6(2)Å^3	
D_x = 1.120 g/cm^3	
No. of observations (all) = 3176	
θ_{max} = 68.2° with Cu K_α	
R(all) = 0.057	
$(\Delta/\sigma)_{max}$ = 0.000	
$(\Delta\rho)_{max}$ = 0.15 e/Å^3	
$(\Delta\rho)_{min}$ = –0.17 e/Å^3	
Measurement: Rigaku RAXIS-RAPID	
Program system: CrystalStructure 3.7.0[3]	
Structure determination: SIR92[4]	
Refinement: full-matrix	
CCDC deposition number: 711786	

† To whom correspondence should be addressed.
E-mail: hirayama@is.icc.u-tokai.ac.jp